Large-scale conformational changes of FhaC provide insights into the two-partner secretion mechanism

G. Sicoli[1*], A. Konijnenberg[2*$], J. Guerin[3$], S. Hessmann[4,5], E. Del Nero[4,5], O. Hernandez-Alba[4,5], S. Lecher[3], G. Rouaut[6], L. Müggenburg[6$], H. Vezin[1], S. Cianférani[4,5], F. Sobott[2,7], R. Schneider[6$£], F. Jacob-Dubuisson[3£]

[1] Laboratoire Avancé de Spectroscopie pour les Interactions, la Réactivité et l'Environnement (LASIRE), UMR CNRS 8516, Université de Lille, Avenue Paul Langevin – C4, F-59655 Villeneuve d'Ascq Cedex, France

[2] BAMS Research group, University of Antwerp, Groenenborgerlaan 171, 2020 Antwerp, Belgium

[3] CNRS, INSERM, Institut Pasteur de Lille, U1019-UMR9017-CIIL-Center for Infection and Immunity of Lille, F-59000, Lille, France

[4] Laboratoire de Spectrométrie de Masse BioOrganique, Université de Strasbourg, CNRS, IPHC UMR 7178, Strasbourg 67000, France

[5] Infrastructure Nationale de Protéomique ProFI – FR2048, 67087 Strasbourg, France

[6] ERL 9002 CNRS Biologie Structurale Intégrative, UMR INSERM 1167, Université de Lille, 50 Avenue Halley, F-59650 Villeneuve d'Ascq, France

[7] Astbury Centre for Structural Molecular Biology and the School of Molecular and Cellular Biology, University of Leeds, Leeds LS2 9JT, United Kingdom

[*] These authors contributed equally.

[£] These authors contributed equally. For correspondence: robert.schneider@univ-lille.fr; francoise.jacob@ibl.cnrs.fr

[$] current addresses: AK, Thermo Fisher Scientific, Zwaanstraat 31 G/H, Building TR, 5651 Eindhoven, The Netherlands; JG, Calixar, 60 avenue Rockefeller, 69008 Lyon, France; LM, Institut für Organische Chemie, Gottfried Wilhelm Leibniz Universität Hannover, Schneiderberg 1B, DE-30167 Hannover, Germany; RS, Bruker Switzerland AG, Industriestrasse 26, CH-8117 Fällanden, Switzerland.

Abstract

The Two-Partner secretion pathway mediates protein transport across the outer membrane of Gram-negative bacteria. TpsB transporters belong to the Omp85 superfamily, whose members catalyze protein insertion into, or translocation across membranes without external energy sources. They are composed of a transmembrane β barrel preceded by two periplasmic POTRA domains that bind the incoming protein substrate. Here we used an integrative approach combining *in vivo* assays, mass spectrometry, nuclear magnetic resonance and electron paramagnetic resonance techniques suitable to detect minor states in heterogeneous populations, to explore transient conformers of the TpsB transporter FhaC. This revealed substantial, spontaneous conformational changes with a portion of the POTRA2 domain coming close to the lipid bilayer and surface loops. Specifically, the amphipathic β hairpin immediately preceding the first barrel strand can insert into the β barrel. We propose that these motions enlarge the channel and hoist the substrate into it for secretion. An anchor region at the interface of the β barrel and the POTRA2 domain stabilizes the transporter in the course of secretion. Our data propose a solution to the conundrum how these transporters mediate protein secretion without the need for cofactors, by utilizing intrinsic protein dynamics.

Introduction

The Two-Partner Secretion (TPS) pathway is dedicated to the export of large proteins notably serving as virulence factors (Guerin et al., 2017). The TpsB transporters are transmembrane β-barrel proteins that secrete their substrates, collectively called TpsA proteins, across the outer membrane of various Gram-negative bacteria. They belong to the ubiquitous Omp85 superfamily whose members mediate protein insertion into, or translocation across membranes of bacteria and

51 eukaryotic organelles, and which includes the essential bacterial BamA transporters (Heinz &
52 Lithgow, 2014; Knowles et al., 2009; Noinaj et al., 2017). The FhaB/FhaC pair of *Bordetella*
53 *pertussis* is a model TPS system, in which the FhaC transporter mediates the translocation of the
54 adhesin FhaB across the outer membrane (Fan et al., 2012).

55 Omp85 transporters are composed of N-terminal POTRA (polypeptide transport associated)
56 domains - two in the case of TpsB transporters - followed by a 16-stranded transmembrane β barrel,
57 which for FhaC is the FhaB translocation pore (Baud et al., 2014). The POTRA domains mediate
58 protein-protein interactions in the periplasm, and notably recognition of client proteins (Delattre
59 et al., 2011). Another hallmark feature of the Omp85 superfamily is the extracellular loop L6 that
60 folds back inside the barrel and harbors a conserved motif at its tip forming a salt bridge interaction
61 with a specific motif of the inner β-barrel wall (Gu et al., 2016; Maier et al., 2015; Noinaj et al.,
62 2013).

63 A specific feature of TpsB transporters is an N-terminal α helix called H1 that plugs the β barrel
64 (Clantin et al., 2007; Guerin et al., 2014; Guerin et al., 2020; Maier et al., 2015) (Fig. 1A, B). An
65 extended linker follows H1 and joins it to the POTRA1 domain in the periplasm. Recently, the X-
66 ray structures of the TpsB transporters $CdiB^{Ab}$ and $CdiB^{Ec}$ have shown very similar folds to that
67 of FhaC, albeit with slightly different positions of H1 in the barrel (Guerin et al., 2020). Both H1
68 and L6 stabilize the barrel in a closed conformation that most likely corresponds to the resting state
69 of the transporter (Guerin et al., 2020; Maier et al., 2015). The β barrel, the L6 loop and the two
70 POTRA domains are essential for transport activity (Clantin et al., 2007).

71 Omp85 transporters likely function in the absence of ATP or an electrochemical gradient. They
72 appear to be very dynamic and to undergo conformational cycling (Doerner & Sousa, 2017; Guerin
73 et al., 2020; Hartmann et al., 2018; Iadanza et al., 2020; Renault et al., 2011; Warner et al., 2017).

74 Lateral opening of the barrel between the first and last anti-parallel β strands is a common
75 mechanistic feature of Omp85 transporters, which is involved in their respective functions
76 (Diederichs et al., 2020; Doyle & Bernstein, 2019; Estrada Mallarino et al., 2015; Guerin et al.,
77 2020; Höhr et al., 2018; Iadanza et al., 2016; Noinaj et al., 2014; Tomasek et al., 2020).

78 The mechanism of two-partner secretion remains poorly understood, but it is known to involve
79 substantial conformational changes of the transporter including exit of H1 from the β barrel and
80 motions of the L6 loop (Guerin et al., 2014; Guerin et al., 2020; Guerin et al., 2015) (Figure 1B).
81 The motion of H1 toward the periplasm is facilitated by conformational changes of flexible regions
82 of the barrel, in particular the first β-barrel strand B1 and the extracellular loops L1, L2 and L6
83 (Guerin et al., 2020). Binding of the N-terminal, conserved 'TPS' domain of the substrate protein
84 to the POTRA domains of its transporter also appears to enhance conformational changes (Guerin
85 et al., 2015). How the substrate enters the pore and is progressively hoisted towards the cell surface
86 without backsliding to the periplasm remains unknown, but we hypothesize a mechanism implying
87 yet uncharacterized transient conformations of TpsB transporters. In this work we have explored
88 such FhaC conformers using biophysical techniques suitable to detect minor states in
89 heterogeneous populations. Our data revealed an intrinsic exchange of the POTRA2 domain
90 between several conformations in slow equilibrium, and that these conformational changes are
91 linked to transport activity.

92

93 **Results**

94 **Effects of freezing the POTRA2 conformation on secretion activity**

95 We have previously obtained evidence that, in addition to the H1 helix and the L6 loop, the
96 POTRA2 domain also undergoes conformational changes during secretion (Guerin et al., 2015).

97 To determine which POTRA2 regions must be mobile for secretion, we searched for specific H
98 bond- or salt bridge-mediated interactions present in the resting conformation (i.e., corresponding
99 to the crystallographic structure) and disrupted them to loosen the structure or conversely replaced
100 them with disulfide (S-S) bonds to limit motions of the corresponding regions. Of note, FhaC is
101 naturally devoid of Cys residues. Residues involved in interactions between the POTRA2 domain
102 and the barrel (Asn^{245}-Ser^{157} and Asn^{245}-Lys^{184}) and in a barrel-distal region of the POTRA2
103 domain (Asp^{165}-Lys^{171}) were replaced with Ala or Cys, and the effects of these mutations on
104 secretion activity were determined (Figure 2A-D). S-S bond formation is catalyzed by the
105 periplasmic disulfide oxidase DsbA in the course of biogenesis, which generally affects SDS-
106 PAGE migration of the protein in the absence of a reducing agent, unless the intervening loop
107 between the Cys residues is too short. The Asn^{245}Ala substitution markedly decreased the activity
108 of FhaC and somewhat reduced its amount in the membrane, unlike formation of Cys^{157}-Cys^{245} or
109 Cys^{184}-Cys^{245} S-S bonds (Figure 2C, D). This indicates that these barrel-POTRA2 interactions
110 contribute to FhaC activity, possibly because they stabilize its conformation in the secretion cycle.
111 On the contrary, the engineered Cys^{165}+Cys^{171} substitutions strongly reduced the level and the
112 activity of FhaC in a *dsbA*$^{+}$ background. Although protein migration was not affected, the S-S
113 bond was most likely formed, since secretion was not reduced in a *dsbA*$^{-}$ background or with the
114 individual substitutions. The observation that S-S bond formation between these two Cys residues
115 is detrimental points to the need for flexibility in the barrel-distal region of the POTRA2 domain.
116

117 **Evidence for dynamics and alternative conformations of FhaC in lipid bilayers by NMR**
118 **spectroscopy**

119 To gain insight into the nature and the time scale of the conformational changes of FhaC, we
120 made use of nuclear magnetic resonance (NMR) spectroscopy for its ability to characterize
121 molecular structure and dynamics as well as minor conformational states of proteins in lipid bilayer
122 environments (Mittermaier & Kay, 2009; Liang & Tamm, 2016). We recorded NMR spectra of
123 FhaC in liposomes and lipid nanodiscs (Bayburt et al., 1998; Viegas et al., 2016), using solid- and
124 solution-state NMR techniques, respectively. To render the 61-kDa protein more accessible to
125 NMR spectroscopy, we resorted to perdeuteration and specific ^{1}H, ^{13}C-isotope labeling of
126 isoleucine (Ile) δ_1 methyl groups (Ruschak & Kay, 2010). Since the 15 Ile residues of FhaC are
127 well distributed across all structural elements of the protein (Figure 3A), we expected this reduced
128 labeling scheme to nevertheless be able to report on larger-scale structural transitions of FhaC.
129 Signals from all Ile residues could be identified and assigned by Ile-to-Val mutations or
130 paramagnetic relaxation enhancement experiments (Fig. 3B; see also below) (Amero et al., 2011;
131 Venditti et al., 2011). The higher resolution of solution-state NMR spectra of FhaC in nanodiscs
132 proved useful in the assignment (Figure 3 Supplement 1). Variable intensities of the Ile δ_1 methyl
133 signals report on local dynamics in the protein. While Ile^{14} in H1 was only visible in scalar
134 coupling-based spectra, the signal of Ile^{548} in β-strand B16 at the barrel seam consistently exhibited
135 low intensity in both scalar and dipolar coupling-based spectra (Figure 3B, Figure 3 Supplement
136 1). This indicates sub-µs time scale motion towards the N-terminus of the H1 helix and µs-to-ms
137 time scale exchange dynamics at the barrel seam, respectively. The notion of dynamics in FhaC is
138 also supported by the absence of through-space correlations for all but the shortest Ile-Ile distances
139 expected from the crystal structure (Figure 3 Supplement 2). However, ^{13}C rotating-frame ($R_{1\rho}$)
140 relaxation dispersion experiments probing exchange between states with different chemical shifts
141 on the µs time scale (Lewandowski et al., 2011; Ma et al., 2014) yielded statistically flat dispersion

142 profiles (Figure 3 Supplement 3), indicating that conformational changes of FhaC detectable by
143 Ile δ_1 methyl chemical shifts must occur on slower time scales.

144 To specifically probe for alternative FhaC conformations, we performed paramagnetic
145 relaxation enhancement (PRE) NMR experiments in which a paramagnetic methanethiosulfonate
146 spin label (MTSL) is attached to an engineered Cys in the protein, and attenuation of NMR signals
147 of nuclei within a radius of about 25 Å around the MTSL probe can be detected even if they only
148 transiently approach the probe (Battiste & Wagner, 2000; Clore & Iwahara, 2009; Nadaud et al.,
149 2007). We chose residue 220 in the extracellular loop L1 for this experiment, yielding $FhaC^{220R1}$,
150 where R1 represents the spin label. Intensities of Ile δ_1 methyl signals in $FhaC^{220R1}$ measured by
151 solid-state NMR in proteoliposomes were referenced to those in a sample with a diamagnetic
152 MTSL analog attached to the same residue, $FhaC^{220R1dia}$ (Fig. 3B, C). Comparison of the signal
153 intensity ratios obtained for different FhaC residues allows to determine whether a signal is more
154 attenuated than would be expected from the crystal structure, indicating a residue approaching the
155 probe more closely (see Methods).

156 In agreement with expectations, residues more than 35 Å away from the position of the
157 paramagnetic MTSL tag modelled onto the FhaC crystal structure (Ile^{114}, Ile^{136}, and Ile^{141} in
158 POTRA1 and POTRA2) exhibited the highest para- versus diamagnetic intensity ratios, while
159 residues expected to be within 16 to 25 Å of the paramagnetic center (Ile^{27}, Ile^{441}, Ile^{506}, Ile^{548})
160 showed attenuation of their NMR signals in paramagnetic $FhaC^{220R1}$ (Figure 3B, C, Figure 3
161 Supplement 4). The overlapped signal corresponding to residues Ile^{252} and Ile^{420}, at expected
162 distances to the paramagnetic center of 12 and 32 Å, respectively, exhibited intermediate
163 attenuation as expected. Signals from the POTRA2 H4 helix (Ile^{172}, Ile^{176}, Ile^{179}) were not
164 significantly attenuated compared to reference signals. However, the signal of Ile^{188} in strand b5

165 of the POTRA2 domain was attenuated more than would be expected for a residue at 35 Å distance
166 from the paramagnetic center. The difference in attenuation with respect to the reference residues
167 Ile^{114}, Ile^{136}, and Ile^{141} is significant ($p < 0.05$, Figure 3C). This result indicates that a region of the
168 POTRA2 domain encompassing strand b5 can approach the extracellular loops of FhaC.
169

170 **Evidence for motions of the POTRA2 domain towards the extracellular side from EPR**
171 **spectroscopy**

172 To complement the NMR data, we resorted to electron paramagnetic resonance (EPR)
173 spectroscopy, another technique suitable to detect dynamics and minor conformational states of
174 proteins in lipid bilayers, but sensitive to longer distances than can be measured by NMR (Sahu &
175 Lorigan, 2020; Torricella et al., 2021). Distances from about 1.8 to 8 nm between paramagnetic
176 spin labels attached to membrane proteins can be measured with pulsed electron double resonance
177 (PELDOR) EPR experiments and can provide insight into non-homogeneous conformational
178 ensembles (Jeschke, 2012). Notably, in continuous-wave (CW) EPR spectroscopy experiments
179 with FhaC carrying a single paramagnetic spin label attached at the solvent-exposed position 195
180 in the POTRA2 domain, we have previously observed a very slow-motion component for the spin
181 probe (Guerin et al., 2015), suggesting possible interactions of the probe with the lipid bilayer in
182 some conformers. To explore this further with explicit distance measurements, we performed
183 PELDOR experiments. We introduced a Cys residue at position 503 in the extracellular L7 loop
184 and combined it with another Cys either at position 195 in the b5-b6 hairpin of the POTRA2
185 domain, position 187 in the b5 strand, or position 33 in the linker, and we labeled both with an
186 MTSL spin label, yielding FhaC variants $FhaC^{33R1+503R1}$, $FhaC^{187R1+503R1}$, and $FhaC^{195R1+503R1}$.

187 In b-octyl glucoside (bOG) micelles, for FhaC$^{195R1+503R1}$ and FhaC$^{187R1+503R1}$, the main populated
188 states correspond to distance distributions between the two spin probes that are consistent with
189 distances calculated using MTSL rotamer libraries attached to the corresponding residues of the
190 FhaC crystal structure (Figure 4A; Figure 4 Supplement 1) (Jeschke, 2013, 2020). For
191 FhaC$^{33R1+503R1}$, a broad distance distribution was observed, with contributions centered at 4.2 nm
192 and 4.6 nm as predicted by rotamer libraries (Figure 4 Supplement 1). In proteoliposomes, for
193 FhaC$^{195R1+503R1}$ and FhaC$^{187R1+503R1}$, the main populated states correspond to long distances of 5 to
194 6 nm between the two spin probes (Figure 4B). Note that these distances are shorter than the
195 expected distances calculated using MTSL rotamer libraries, since the lipid environment limited
196 the dipolar evolution times that could be applied in PELDOR experiments (Figure 4 Supplement
197 2). In addition to the expected long inter-spin distance, shorter distance distributions centered at
198 2.5 nm and 3.5 nm were observed for FhaC$^{195R1+503R1}$ (Figure 4B). They can be attributed to
199 conformers with the two spin probes closer to one another than in the crystal structure
200 conformation. Similarly, additional peaks corresponding to shorter-than-expected distances were
201 observed in the distance distributions for FhaC$^{187R1+503R1}$ (Figure 4B). These results strongly
202 support the idea that the b5-b6 hairpin of the POTRA2 domain moves towards the extracellular
203 surface of FhaC in some conformers. For FhaC$^{33R1+503R1}$, distances both shorter and longer than
204 expected were obtained. This indicates that, in addition to moving away from the membrane when
205 H1 exits from the pore, as reported in (Guerin et al., 2014), the linker also moves toward the surface
206 in specific conformers.

207 The point mutation Asp^{492}Arg disrupts a conserved salt bridge between L6 and the inner barrel
208 wall and induces conformational changes in FhaC (Guerin et al., 2015). To determine whether it
209 affects the conformational equilibrium of the POTRA2 domain, we introduced the Asp^{492}Arg

210 substitution in FhaC$^{195R1+503R1}$. Indeed, PELDOR experiments showed an increased proportion of
211 species characterized by short inter-spin distances in this mutant (Figure 4 Supplement 3).
212 Notably, we did not obtain indications for alternative conformers in FhaC reconstituted into
213 nanodiscs with EPR or NMR spectroscopy. Analysis of PELDOR experiments on FhaC$^{195R1+503R1}$
214 in nanodiscs yielded only a long distance between the spin labels, as expected from the crystal
215 structure, and PRE experiments on FhaC^{195R1} in nanodiscs showed attenuation of NMR signals
216 only within the POTRA2 domain (Figure 4 Supplement 4). Along with smaller linewidths of FhaC
217 NMR signals in nanodiscs compared to liposomes (Figure 3 Supplement 1), these findings indicate
218 that the constrained nanodisc environment limits the conformational space accessible to FhaC and
219 hinders the larger-scale conformational changes that can be observed in proteoliposomes.
220 Taken together, both our EPR and NMR data show that the POTRA2 domain can undergo large
221 conformational changes that bring its b5-b6 hairpin close to the membrane and the extracellular
222 side, and that these conformational changes are facilitated by the rupture of the interaction between
223 L6 and the inner barrel wall. The H1-POTRA1 linker can also adopt alternative conformations and
224 notably move towards the cell surface.
225
226 ***In vivo* evidence for conformers with the POTRA2 domain or the linker close to surface loops**
227 To investigate whether the conformers observed in proteoliposomes also exist *in vivo* and to obtain
228 insight into the potential position of the POTRA2 domain in those conformers, we simultaneously
229 replaced two residues distant in the X-ray structure of FhaC with Cys residues to detect
230 spontaneous S-S bond formation. Our rationale was that conformational changes that bring the two
231 Cys residues close to each other should promote S-S bond formation even if the corresponding
232 alternative conformations are short-lived, as the S-S bound species accumulate over time. These

233 experiments were performed in a *dsbA*$^{-}$ background, such that S-S bonds formed after FhaC
234 biogenesis and thus exclusively resulted from its conformational changes in the membrane. We
235 combined Cys residues at the extracellular surface at positions 224 in L1, 290 in L3, 342 in L4,
236 391 in L5, 503 in L7 or 545 in L8 with periplasmic Cys residues in the POTRA2 domain at
237 positions 167, 176 or 195, in the linker at position 48, or in the POTRA1 domain at position 86
238 (Figure 5A). None of the single Cys substitutions markedly affected the secretion activity of FhaC
239 (Baud et al., 2014; Guerin et al., 2014; Guerin et al., 2015). Under non-reducing conditions, partial
240 oxidation of FhaC as detected by aberrant migration in SDS-PAGE was identified for the
241 combinations Cys^{195}+Cys^{224}, Cys^{176}+Cys^{224}, Cys^{48}+Cys^{224}, Cys^{48}+Cys^{545} and weakly for
242 Cys^{167}+Cys^{224}, indicating S-S bond formation within specific pairs of engineered Cys residues
243 (Figure 5B). In contrast, no loop other than L1 or L8 was found to cross-link with those periplasmic
244 regions, and none cross-linked with the Cys residue in the POTRA1 domain. To confirm S-S bond
245 formation, the $FhaC^{C48+C224}$ and $FhaC^{C195+C224}$ variants were overexpressed, purified and subjected
246 to liquid chromatography coupled to tandem mass spectrometry (MS) in reducing and non-
247 reducing conditions. In both variant samples, the regions that contain the Cys residues were
248 detected only when proteolytic digestion was performed after reduction and alkylation (Figure 5
249 Supplement 1), which supports S-S bond formation between the linker and L1 in $FhaC^{C48+C224}$ and
250 between the POTRA2 domain and L1 in $FhaC^{C195+C224}$. Thus, *in vivo*, the last portion of the linker
251 can be found close to the extracellular loops L1 and L8 that immediately follow and precede the
252 first and last β–barrel strands, B1 and B16, respectively, and the α helix H4 and the b5-b6 β hairpin
253 of the POTRA2 domain can be found close to the extracellular loop L1. This indicates that these
254 periplasmic elements approach the β–barrel seam in specific conformers, in agreement with our *in*
255 *vitro* data.

256

257 **Interactions of portions of the POTRA2 domain with the β barrel by native mass**
258 **spectrometry**

259 Our data imply that the POTRA2 domain undergoes some breaking up in the secretion cycle. We
260 thus investigated its lability by using structural MS-based approaches (Figure 6). Native MS
261 analysis of FhaC revealed a monomer that could be stripped of bOG at 60 V, a relatively low
262 collision energy (CE), and that displayed a narrow charge state distribution between 14+ and 19+
263 indicative of a folded protein in a single conformation (Figure 6 A, B, Figure 6 Supplement 1).

264 We used collision-induced unfolding (CIU) (Tian et al., 2015) to characterize the stability and
265 the organization of the FhaC domains. FhaC displayed two transitions at 60 V and 120 V as shown
266 by the increases of collision cross section (CCS) values (Figure 6C). As the number of transitions
267 in the gas phase can generally be related to the number of domains of a protein (Zhong et al., 2014),
268 and extra-membrane domains are more likely to experience early unfolding than domains
269 embedded in detergent or lipids due to collisional cooling (Barrera et al., 2009), those transitions
270 might be caused by unfolding of the POTRA domains and/or ejection and unfolding of H1. Control
271 CIU experiments with other *B. pertussis* outer membrane proteins (OMPs) with small soluble
272 domains inside their β barrels, the TonB-dependent transporter BfrG and the translocator domain
273 of an autotransporter, SphB1-αβ, showed a single unfolding transition at low voltage, which likely
274 corresponds to unfolding of these soluble domains (Figure 6 Supplement 2). Thus, the β barrels of
275 these three proteins likely remain structurally intact at high activation conditions, most likely due
276 to strong hydrogen bonding networks.

277 To further investigate whether the CIU transitions observed for FhaC stem from unfolding of
278 the POTRA domains or ejection of the H1 helix, we studied the CIU pathway of $FhaC^{C4+C391}$ in

279 which H1 is locked inside the barrel by an S-S bond and thus cannot move out (Guerin et al., 2014).
280 FhaC$^{C4+C391}$ exhibited the same transitions as wt FhaC, although the second unfolding event was
281 delayed by 30 V and the overall CCS value was increased by 50 Å^2 (Figure 6 Supplement 3). As
282 CIU is unlikely to break S-S bonds (Tian et al., 2015), comparison of these unfolding pathways
283 suggests that the two transitions correspond to successive unfolding of the POTRA domains, with
284 the barrel remaining intact in those conditions. H1 stays inside the barrel or its unfolding barely
285 registers in the CCS values. The delay of the second unfolding transition for FhaC$^{C4+C391}$ suggests
286 that locking H1 in the barrel stabilizes one of the POTRA domains, although from the data we
287 cannot discern which one.

288 We next tested the possibility that portions of the POTRA2 domain might bind to the β barrel,
289 probably along strands B1 or B16 upon opening of the barrel seam. Using native MS, we assessed
290 the binding of synthetic peptides that correspond to various periplasmic portions of FhaC,
291 including b5-b6, b4+L (*i.e.*, b4 followed by the b4-H3 linker) and L+H4 (*i.e.*, the H3-H4 linker
292 followed by H4) of the POTRA2 domain, b2-b3 of the POTRA1 domain, Lk, a non-structured
293 peptide from the linker region between H1 and the POTRA1 domain, and the N-terminal β hairpin
294 of the FhaB transport substrate, Fha-NT (Figure 7; Figure 7 Supplement 1). The same experiments
295 were performed with SphB1-αβ to correct for non-specific binding, which might occur in native
296 MS experiments due to artifacts induced by interaction with the detergent during the electrospray
297 process (Landreh et al., 2016). Fha-NT, b4+L and b5-b6 exhibited binding to FhaC, with b5-b6
298 binding at the highest level and in two copies, but markedly less to the FhaC$^{C4+C391}$ variant (Figure
299 7A; Figure 7 Supplement 2). In contrast, the peptides containing the sequences of b2-b3 of the
300 POTRA1 domain, H4 or the H1-POTRA1 linker did not bind.

301 We assessed structural changes induced by peptide binding using native ion-mobility (IM)
302 MS. At low CE (*i.e.*, no activation), all three peptides increased the CCS of the compact state of
303 FhaC by rather small increments of 91-92 $Å^2$ (Figure 7B, C; Figure 7 Supplement 3). However,
304 upon increasing the activation conditions, Fha-NT and b4+L no longer increased the CCS of FhaC,
305 compared to the unbound protein. In contrast, the b5-b6 peptide caused an increase in CCS values
306 both at low and high collisional activation, suggesting that a structural change was induced upon
307 peptide binding and that the peptide was bound to a region that remains folded in these conditions
308 (Figure 7B, C, Figure 7 Supplement 4). As our CIU studies suggest that the POTRA domains likely
309 unfold at high CE, the effect of b5-b6 on the CCS might thus stem from peptide binding to the β
310 barrel. The same experiment with $FhaC^{C4+C391}$ showed a lower level of peptide binding, which
311 nevertheless caused a similar increase of CCS at both low and high energies, like with wt FhaC
312 (Figure 6 Supplement 3, Figure 7 Supplement 4). This supports the model that the peptide
313 corresponding to the b5-b6 hairpin of the POTRA2 domain interacts with the β barrel, and that
314 this interaction is facilitated by the ejection of H1. Given the amphipathic nature of this hairpin, it
315 most likely aligns with an edge of the open β-barrel seam, consistent with the cross-linking data.

316

317 **DISCUSSION**

318 As Omp85 transporters are thought to perform their functions in the absence of an energy source
319 in the periplasm, their postulated conformational cycling must involve low energy barriers between
320 conformers, as reported for BamA (Xiao et al., 2021). Here, we obtained evidence for large
321 conformational changes of FhaC that involve portions of the POTRA2 domain approaching the
322 extracellular side of the protein. Conformational changes of FhaC occur independently of the
323 presence of the substrate, indicating that such dynamics is an intrinsic structural feature of the

324 protein, with implications for its function. Notably, the conformational states appear to be in slow
325 equilibrium, as with BamA (Hartmann et al., 2018).

326 All structural elements of TpsB transporters are connected with one another, structurally and
327 functionally, and their motions appear to be coupled (Guerin et al., 2014; Guerin et al., 2020;
328 Guerin et al., 2015; Maier et al., 2015). In the resting conformation, H1 and L6 interact with the
329 barrel wall, H1 with L1, the H1-POTRA1 linker with the POTRA domains, and the POTRA2
330 domain with the periplasmic side of the barrel (Guerin et al., 2020; Maier et al., 2015). In the
331 secretion process, L6 breaks its connection with the barrel wall, H1 moves towards the periplasm,
332 and part of the B1-B16 seam unzips (Guerin et al., 2014; Guerin et al., 2020; Guerin et al., 2015).
333 In the current work we have obtained evidence fur further conformational changes involving the
334 POTRA2 domain. Thus, EPR, NMR and S-S cross-linking data revealed the proximity of parts of
335 the POTRA2 domain to the barrel seam and to the extracellular side of FhaC in specific conformers,
336 and structural MS experiments showed the binding of the POTRA2 b5-b6 hairpin peptide to the
337 β barrel under conditions in which the POTRA domains are very likely unfolded.

338 Based on these and previous data, we propose the following model for the first steps of secretion
339 (Figure 8). The closed, resting conformation of FhaC is in slow equilibrium with an open
340 conformation in which L6 has been released from its interaction with the barrel wall and H1 has
341 moved out of the pore (Figure 8A) (Guerin et al., 2014; Guerin et al., 2020; Guerin et al., 2015).
342 In the open conformation, the linker has vacated the substrate binding site on the POTRA2 domain,
343 thus enabling a specific portion of the conserved TPS domain of the substrate to bind to the groove
344 between H4 and b5 (Delattre et al., 2011). According to molecular dynamics simulations, the exit
345 of H1 facilitates barrel unzipping between B1 and B16 (Guerin et al., 2020). Barrel unzipping is
346 coupled with a swing motion of the b5-b6 hairpin of the POTRA2 domain towards the barrel,

347 followed by its binding to the open seam, probably by β augmentation, thus enlarging the barrel
348 and hoisting the bound substrate into the channel (Figure 8B).

349 The next secretion steps are more speculative. The entropic cost of confining a portion of the
350 bound, unfolded polypeptide inside the channel might facilitate its diffusion toward the surface
351 (Halladin et al., 2021). The TPS domain most likely forms a hairpin inside the barrel, as proposed
352 previously (Nash & Cotter, 2019), and a specific region binds to the extracellular β sheet formed
353 by B5-B8 (Baud et al., 2014), which might template the folding of the substrate into a nascent β
354 helix. The substrate would progressively be threaded across the channel and fold at the surface,
355 leading to the formation of a stable β helix nucleus (Alsteens et al., 2013), which would prevent
356 backtracking of the protein chain, effectively adding directionality to its stochastic motion as
357 proposed by the "Brownian ratchet" mechanism (Peterson et al., 2010). According to our model,
358 TpsB transporters mediate protein secretion without the need for cofactors by utilizing intrinsic
359 protein dynamics. Although the conformational changes we describe are unprecedented in the
360 Omp85 superfamily, divergent functional evolution has necessarily led to specific mechanistic
361 adaptations. Recent work has indicated that energy may be transduced from the inner membrane
362 to the BAM complex through the protonmotive force-utilizing SecDF complex (Alvira et al., 2020).
363 One cannot rule out that the intrinsic conformational changes of FhaC *in vivo* are similarly
364 enhanced by an energy-transducing mechanism.

365 The b5-b6 hairpin most likely binds by β augmentation of the barrel strand B1, by analogy with
366 BamA and Sam50 in which the unzipped B1 strand templates folding of client proteins by β
367 augmentation (Doyle & Bernstein, 2019; Höhr et al., 2018; Tomasek et al., 2020; Wu et al., 2021).
368 This mode of binding is supported by our CIU results showing an increased cross-section of the
369 protein upon binding of b5-b6 to the barrel and by the *in vivo* formation of an S-S bond between

370 the tip of that hairpin and the extracellular loop L1. The b5-b6 sequence, with its amphipathic
371 nature and suitable charge partitioning, fits ideally in the open seam. The observation that portions
372 of the linker may approach the extracellular loops likely reflects futile conformational changes
373 involving the linker bound to the POTRA2 being hoisted into the channel in place of the substrate,
374 in the absence of the latter (Figure 8C). Notably, evidence for the C-terminal portion of the linker
375 reaching the cell surface was obtained previously (Guedin et al., 2000).

376 As the POTRA2 domain partially breaks up during secretion, it must reassemble after secretion
377 is completed. This may be mediated by the interactions of the H3 helix and the barrel-proximal
378 end of b5 of the POTRA2 domain with the periplasmic turn T1 of the barrel, which are important
379 for FhaC activity. These fixed points of the POTRA2 domain may ensure that FhaC can regain its
380 resting conformation after secretion, which is necessary to limit outer membrane permeability.
381 Consistent with this hypothesis, disrupting the conformation of the periplasmic turn T1 yielded
382 transient, very large channels as detected in electrophysiology experiments (Méli et al., 2006).
383 Stabilizing specific conformations of the transporter might also account for the importance of the
384 interaction between L6 and the inner barrel wall (Delattre et al., 2010).

385 In summary, we propose a novel mechanism of protein transport in TPS systems based on
386 large-scale, spontaneous conformational dynamics of the TpsB partner. Our model integrates and
387 explains currently available data from several complementary *in vitro* and *in vivo* approaches and
388 establishes mechanistic links between TpsBs and other Omp85 transporters.

389

390 **Materials and Methods**

391 **Strains and plasmids**

392 *E. coli* JCB570 or JCB571 (*dsbA*::kan) were used for low level expression of FhaC and *E. coli*
393 BL21(DE3-*omp5*) for overexpression. For peptide mapping $FhaC^{C48+C224}$ and $FhaC^{C195+C224}$ were
394 overexpressed in BL21(DE3-*omp5 dsbA::kan*), which was constructed as described in (Derbise et
395 al., 2003). Point mutations in *fhaC* were generated using the QuikChange II XL Kit (Agilent, Les
396 Ulis, France) on pFc3 (Guedin et al., 2000). Overexpression of FhaC for purification was
397 performed from pET22 or pET24 plasmids (Clantin et al., 2007). ptacFha44-His codes for the first
398 80 kDa of the FhaC substrate FhaB, called Fha44, followed by a 6-His tag. It was constructed by
399 adding a 1.2-kb Sal-BamHI fragment of the *fhaB* gene into the same sites of ptacNM2lk-His
400 (Guerin et al., 2015). pFJD63 codes for FhaC under the control of the P_{BAD} promoter (Guedin et
401 al., 1998). Its derivatives were constructed by ligating the XhoI-HindIII and XhoI-XbaI fragments
402 of pFJD63 with the XbaI-HindIII *fhaC* fragments carrying the relevant mutations from the pFc3
403 derivatives. pMSP1D1 and pMSP1E3D1 were obtained from Addgene (Watertown, MA, USA).
404 pSphB1αβ is a derivative of pT7SBαβ (Dé et al., 2008) with a 6-His tag. To construct pT7bfrG-
405 H, the sequence corresponding to the mature protein was PCR amplified and inserted in pFJD138
406 (Méli et al., 2006) after the signal-peptide and 6-His tag sequences.
407
408 ***In vivo* assays**
409 To monitor S-S bond formation *in vivo*, the pFc3 variants were introduced in *E. coli* JCB571. The
410 recombinant bacteria were grown at 37°C in minimum M9 medium containing 0.1%
411 casaminoacids under agitation. The cells were collected by centrifugation when the optical
412 densities at 600 nm (OD_{600}) of the cultures reached 0.8. The cell pellets were resuspended in 50
413 mM sodium (pH 6.8) containing 10 mM N-ethylmaleimide and lysed using a Hybaid ribolyzer
414 apparatus (50 sec at speed 6). The membranes were collected by ultracentrifugation of the clarified

415 lysates at 90,000 g for 1 h. The pellets were resuspended in loading buffer without reducing agent
416 and separated into two aliquots, with DTE added at 25 mM to one of them before heating at 70°C
417 for 10 min. FhaC was detected using anti-FhaC antibodies (Delattre et al., 2011) with alkaline
418 phosphatase development for 15 min.

419 For the secretion assays, overnight cultures of *E. coli* JCB570 or JCB571 harboring a pFJD63
420 derivative and ptacFha44-His were diluted to OD_{600} of 0.3 in LB and grown under agitation with
421 0.01% arabinose for 20 min to produce FhaC. The bacteria were collected by centrifugation,
422 resuspended in prewarmed LB without arabinose and grown to OD_{600} of 0.8 before adding IPTG
423 at 1 mM to induce the expression of Fha44. Culture aliquots were collected 5 and 20 min thereafter
424 and placed on ice. After centrifugation to harvest the bacteria, Fha44 was affinity-purified from
425 the supernatants with Ni-NTA beads (Qiagen, Courtaboeuf, France). The membrane extracts were
426 prepared and FhaC was detected as above. Fha44 was detected by immunoblotting using anti-6His
427 antibodies, the ECL kit of Amersham (Merck, St Quentin-Fallavier, France) and the Amersham
428 Imager 600 (GE) with 1 sec exposure. The amounts of Fha44 in supernatants were quantified with
429 ImageJ.

430

431 **Protein Purification and spin labeling**

432 The production and purification of the FhaC derivatives was performed as described (Guerin et al.,
433 2014). Expression for NMR experiments was performed in M9 minimal medium in D_2O, 2.5 g/L
434 ^{2}H-glucose (Sigma, St Quentin-Fallaviers, France), 1g/L ^{15}N-NH4Cl, 1g/L ^{15}N,^{2}H-isogro (Sigma)
435 and ^{13}C-α-ketobutyric acid (Sigma) to achieve u-(^{2}H,^{15}N), Ile-δ_1($^{13}CH_3$) isotope labeling (Ruschak
436 & Kay, 2010). For spin labeling, 3 mM tris(2-carboxyethyl)phosphine (TCEP, Sigma) was added
437 to the detergent extract before ion exchange chromatography. The FhaC-containing fractions were

438 mixed with a 10-fold molar excess (1-oxyl-2,2,5,5-tetramethyl-Δ3-pyrroline-3-methyl)
439 methanethiosulfonate (MTSL) or its diamagnetic analogue (1-Acetoxy-2,2,5,5-tetramethyl-δ-3-
440 pyrroline-3-methyl) methanethiosulfonate (Toronto Research Chemicals, North York, ON,
441 Canada) at 15°C with gentle agitation for 16 hours. Excess MTSL was removed by
442 chromatography. SphB1-αβ and BfrG were produced from *E. coli* BL21(DE3-*omp5)* and purified
443 from bOG extracts using Ni^{2+} affinity chromatography. For BfrG 300 mM NaCl was added to
444 improve solubility.
445
446 **Preparation of liposomes and nanodiscs and protein reconstitution**
447 Small unilamellar vesicles (SUVs) of *E. coli* polar lipids were prepared as described (Guerin et al.,
448 2014). The SUVs were mixed with FhaC variants at lipid:protein molar ratios of approx. 2500:1
449 for EPR and 200:1 for NMR experiments, respectively, at room temperature, with gentle agitation
450 for one hour. The proteoliposomes were formed by removal of detergent with the progressive
451 addition of Biobeads SM2 (Bio-Rad), and the proteoliposomes were collected by
452 ultracentrifugation. All steps were performed under argon. Final buffer concentrations after mixing
453 FhaC and liposomes were about 12.5 mM each of Tris-HCl and NaP_i, 150 mM NaCl, pH 6.7.
454 Nanodiscs were prepared with the MSP1D1 and MSP1E3D1 scaffold proteins (Ritchie et al.,
455 2009) produced in *E. coli* BL21(DE3), with an induction of 3 h at 28°C. For NMR experiments,
456 scaffold proteins were expressed in M9 minimal medium in D_2O using ^2H-glucose as carbon
457 source to suppress their signals in the (^1H,^{13}C)-based NMR spectra. The bacteria were broken using
458 a French press in 50 mM Tris-HCl (pH 8), 300 mM NaCl (TN buffer), 1% Triton X100 (TNX
459 buffer), and the clarified lysates were subjected to Ni^{2+} affinity chromatography. After successive
460 washes in TNX, TN buffer with 50 mM cholate, 20 mM and 50 mM imidazole, the proteins were

461 eluted in TN buffer with 400 mM imidazole, concentrated by ultrafiltration and dialyzed against
462 20 mM Tris-HCl (pH 8), 200 mM NaCl and 0.1 mM EDTA. Dimyristoyl phosphatidyl choline
463 (DMPC) and dimyristoyl phosphatidyl glycerol (DMPG) (Avanti, Interchim, Montluçon, France)
464 at a 2:1 ratio were solubilized in chloroform, lyophilized overnight and resuspended to 25 mM in
465 20 mM Tris-HCl (pH 7.5), 100 mM NaCl, 0.5 mM EDTA, 50 mM cholate. For NMR experiments,
466 deuterated (d_{54}-) DMPC and DMPG (Cortecnet, Voisins-le-Bretonneux, France) were used. FhaC,
467 the scaffold protein and the lipids were mixed at a ratio of 1:3:180, cholate was added to 15 mM,
468 and incubation was performed for 1 h at room temperature. Biobeads were added progressively,
469 and the incubation was continued at 4°C overnight. The nanodiscs were collected by
470 ultracentrifugation and concentrated by ultrafiltration. For NMR experiments, the buffer was
471 exchanged to 100 mM NaP_i in D_2O pH* 7.2 using a 2-ml ZebaSpin column (7 kDa MWCO).
472

473 **NMR experiments**

474 For solid-state NMR experiments on FhaC variants reconstituted into liposomes, the
475 proteoliposomes collected by ultracentrifugation were transferred to 1.3 mm magic-angle-spinning
476 (MAS) solid-state NMR rotors (Bruker Biospin, Wissembourg, France) using an
477 ultracentrifugation device (Bertini et al., 2012) (Giotto Biotech, Sesto Fiorentino, Italy) in a
478 Beckman ultracentrifuge (SW 32 Ti rotor, 77,000 x g, 12°C, 30 – 60 min). NMR experiments were
479 performed on spectrometers operating at 800 and 950 MHz ^{1}H Larmor frequency (18.8 and 22.3
480 T magnetic field) (Bruker Biospin) at a MAS frequency of 50 kHz. Sample temperature was kept
481 at about 17°C as judged by the chemical shift of the bulk water resonance. Spectra were indirectly
482 referenced to 2,2-dimethyl-2-silapentane-5-sulfonate (DSS) via the lipid methylene proton
483 resonance, which appears at 1.225 ppm under our experimental conditions. Typical pulse lengths

484 for ^{1}H and ^{13}C hard 90° pulses were 2.1 and 3.8 μs, respectively. For cross-polarization (CP), field
485 strengths were 21 and 30 kHz for ^{1}H and ^{13}C, respectively (n=1 double-quantum Hartmann-Hahn
486 condition), with a 50-to-100% ramp on the ^{1}H radiofrequency (RF) field and a duration of 1.5 ms.
487 ^{1}H-detected 2D ^{13}C-^{1}H dipolar hCH correlation spectra (Barbet-Massin et al., 2014) were typically
488 recorded with 1600 data points and a spectral width of 40 ppm in the direct ^{1}H dimension and 100
489 to 140 data points and a spectral width of 13 ppm in the indirect ^{13}C dimension. For water
490 suppression, the MISSISSIPPI scheme (Zhou & Rienstra, 2008) at 15 kHz ^{1}H RF field with a
491 duration of typically 200 ms was employed. For the 2D hChH correlation spectrum, a ^{1}H-^{1}H
492 mixing time of 6.4 ms using radio frequency driven recoupling (Bennett et al., 1992) with a ^{1}H
493 field strength of 120 kHz was applied between back-CP and acquisition. ^{13}C $R_{1\rho}$ spectra
494 (Lewandowski et al., 2011; Ma et al., 2014) were recorded in a pseudo-3D fashion, with the ^{13}C
495 spinlock period inserted between the initial CP and the ^{13}C indirect evolution of the hCH sequence.
496 Spinlock field strengths from 1.2 to 10 kHz were used, and 5 spinlock durations from 2.5 to 80 ms
497 with one repeated value were recorded for each spinlock. The spinlock carrier frequency was kept
498 at the center of the isoleucine δ_1 methyl ^{13}C region, as in all other hCH correlation spectra. A ^{1}H
499 180° pulse was inserted in the middle of the spinlock period to suppress chemical shift anisotropy
500 / dipolar coupling cross-correlated relaxation (Kurauskas et al., 2016). Solid-state PRE NMR
501 experiments were recorded on FhaC samples with either a paramagnetic MTSL tag or a
502 diamagnetic MTSL analogue (Nadaud et al., 2007) attached to a Cys, reconstituted into *E. coli*
503 polar lipid liposomes. Standard dipolar 2D hCH correlation spectra were recorded.

504 Solution-state NMR experiments on FhaC in nanodiscs were conducted on a 900 MHz
505 spectrometer (Bruker Biospin) at 32°C sample temperature. Standard ^{13}C-^{1}H heteronuclear
506 multiple-quantum coherence (HMQC) or SOFAST-HMQC (Schanda & Brutscher, 2005)

experiments were recorded with 2048 and 150 data points and spectral widths of 14 and 7.4 ppm in direct ^{1}H and indirect ^{13}C dimensions, respectively. For PRE experiments, standard ^{13}C-^{1}H HMQC spectra were recorded on a FhaC^{195R1} sample before and after reduction of the paramagnetic MTSL tag with a 10-fold molar excess of ascorbic acid (Battiste & Wagner, 2000).

NMR spectra were processed with TopSpin 4.0.3 (Bruker Biospin) or NMRPipe (Delaglio et al., 1995) and analyzed with Sparky (Lee et al., 2015) or CcpNMR (Vranken et al., 2005). For the relaxation dispersion curves, effective transverse relaxation rates $R_{2,\mathrm{eff}}$ (comprising intrinsic transverse relaxation rate $R_{2,0}$ and any exchange contribution R_{ex}) were extracted from experimental $R_{1\rho}$ values using separately recorded R_1 experiments (Palmer & Massi, 2006). For PRE experiments, ratios of peak intensities in spectra of para- and diamagnetic species (FhaC^{220R1} and FhaC^{220R1dia} for solid-state experiments, oxidized and reduced FhaC^{195R1} in case of the solution-state experiments, respectively) were calculated. These para- versus diamagnetic signal intensity ratios do not normalize to 1 in our case. In the solid-state experiments, this is most likely due to variations between the samples in terms of efficiency of protein reconstitution into liposomes and total amounts of sample transferred to the NMR rotor. Both in solid and solution state, spectroscopic factors likely also play a role (incomplete longitudinal relaxation and thus lower signal-to-noise in the spectra of diamagnetic samples due to the use of short inter-scan delays of 1 s (Iwahara et al., 2007)). We have thus opted to normalize PRE ratios to the maximum ratio observed in each experiment, which was always observed in one of the residues furthest from the paramagnetic center (Ile^{136} in FhaC^{220R1}, Ile^{14} in FhaC^{195R1}). This is equivalent to normalizing signals within each spectrum to a reference signal whose intensity is unaffected by PRE effects. We then only analyzed relative signal attenuation levels, instead of attempting to extract quantitative distance measures. Error bars of PRE intensity ratios were calculated based on spectral

530 noise levels (root-mean-standard deviation of the spectral noise) using standard error propagation.
531 To estimate expected distances between FhaC Ile residues and the MTSL label on residue 220,
532 and consequently relative PRE attenuation levels, an ensemble of 200 MTSL conformations
533 compatible with labeling on FhaC residue 220 was calculated using the mtsslSuite web server
534 (Hagelueken et al., 2015; Hagelueken et al., 2012) (http://www.mtsslsuite.isb.ukbonn.de/) and the
535 FhaC crystal structure (PDB 4QKY) with residue 220 changed to Cys in PyMOL (The PyMOL
536 Molecular Graphics System. Schrödinger, LLC). The average position of the paramagnetic center
537 (taken as halfway between nitrogen and oxygen atoms of the MTSL nitroxide ring) was calculated
538 from the coordinates of these 200 conformations; distances from that position to Ile Cδ1 nuclei
539 were calculated using PyMOL.
540

541 **EPR Experiments**

542 PELDOR experiments were performed at Q-band frequency (~34 GHz) using a Bruker
543 EleXsys E580 spectrometer equipped with an overcoupled Bruker EN 5107D2 resonator. Pulses
544 were generated with a Bruker SpinJet AWG and amplified with a 50 W TWT amplifier. The
545 experiments were performed at 50 K and 30 K using a variable-temperature cryogen-free system
546 (Oxford, Oxford, UK). The deadtime-free, four-pulse PELDOR sequence [(π/2)probe — τ1 —
547 (π)probe — τ1 + t — (π)pump — τ2 –t — (π)probe — τ2 — (echo)] was employed with a 200-ns
548 τ1 delay and τ2 delays ranging from 3,200 ns to 7,000 ns depending on the sample (Pannier et al.,
549 2000). Probe pulses were 10 ns (π/2) and 20 ns (π) Gaussian-shaped pulses at a frequency
550 corresponding to the maximum of the resonator response function and a magnetic field value
551 corresponding to the high-field shoulder of the echo-detected field-swept spectrum. The pump
552 pulse was implemented as a 24-ns pulse centered at a frequency 55 MHz higher than the probe

553 frequency and corresponding to the maximum of the nitroxide field-swept spectrum. Raw time-
554 domain PELDOR traces were background-corrected using the DeerAnalysis 2019 package
555 (Jeschke et al., 2006), and the resulting signals were power-scaled in MATLAB to suppress sum
556 and difference peaks arising from multispin effects. Distance distributions were then calculated
557 from the scaled and background-corrected PELDOR traces by Tikhonov regularization. For
558 $FhaC^{33R1+503R1}$, $FhaC^{187R1+503R1}$ and $FhaC^{195R1+503R1}$, distance distributions were predicted using a
559 pre-computed rotamer library of the MTSL spin probe attached to specific residues on the PDB
560 structure (Jeschke, 2020).
561

562 **Mass fingerprinting of FhaC variants**

563 Purified $FhaC^{C48+C224}$ and $FhaC^{C195+C224}$ variants were subjected to non-reducing SDS-PAGE, and
564 acrylamide bands corresponding to the oxidized forms of the two proteins were excised. They were
565 washed with 50 µL of acetonitrile (ACN)/NH_4HCO_3 (75/25) four times and dehydrated with ACN,
566 or incubated in 10 mM DTT in NH_4HCO_3 for 30 min at 57°C and 30 min room temperature,
567 followed by incubation in 55 mM iodoacetamide in 25 mM NH_4HCO_3 for 20 min in the dark, 3
568 washes with NH_4HCO_3 and dehydration with ACN performed twice. The pH of the samples was
569 decreased to 2.0, digestion was performed with pepsin (0.01 µg/µL) (Promega, Charbonnieres-les-
570 Bains, France) at a 1:50 enzyme:substrate ratio at 37°C for 3 hours, and the reaction was stopped
571 by heating at 95°C for 10 min.

572 NanoLC-MS/MS analysis was performed using a nanoAcquity Ultra-Performance-LC (Waters,
573 Manchester, UK) coupled to a Q-Exactive Plus Orbitrap mass spectrometer (Thermo Scientific,
574 Illkirch, France). Peptides were trapped on a nanoACQUITY UPLC precolumn (C18, 180 µm x
575 20 mm, 5 µm particle size), and eluted from a nanoACQUITY UPLC column (C18, 75 µm x 250

576 mm, 1.7 µm particle size) at a constant temperature of 60°C. Mobile phases A and B were
577 composed of 0.1% formic acid in water and 0.1% formic acid in ACN, respectively. Peptides were
578 eluted with gradients of B from 1 to 8% for 2 min, 8 to 35% for 58 min, 35 to 90% for 1 min, 90%
579 for 5 min, 90 to 1% B for 1 min and a concentration of 1% B for 20 min, with a constant flow rate
580 of 400 nL/min. The source temperature of the mass spectrometer was set to 250°C and the spray
581 voltage at 1.8 kV. Full scan MS spectra were acquired in positive mode with a resolution of
582 140,000, a maximum injection time of 50 ms, and an AGC target value of $3x10^6$ charges. The 10
583 most intense multiply charged peptides per full scan were isolated using a 2 m/z window and
584 fragmented using higher energy collisional dissociation (normalized collision energy of 27).
585 MS/MS spectra were acquired with a resolution of 17,500, a maximum injection time of 100 ms
586 and an AGC target value of 1×10^5, and dynamic exclusion was set to 60 sec. The system was
587 fully controlled by XCalibur software v3.0.63, 2013 (Thermo Scientific) and NanoAcquity UPLC
588 console v1.51.3347 (Waters). The MS/MS data were interpreted using a local Mascot server with
589 MASCOT 2.5.0 algorithm (Matrix Science, London, UK). Spectra were searched with a mass
590 tolerance of 5 ppm for MS and 0.07 Da for MS/MS data, using none as enzyme. Oxidation (+15.99
591 Da), and carbamidomethylation (57.02 Da) were specified as variable modifications. Protein
592 identifications were validated with a Mascot ion score above 25.
593

594 **Native MS and ion mobility**

595 Purified FhaC was buffer exchanged into 100 mM ammonium acetate buffer, pH 6.8,
596 supplemented with 50 mM bOG using a P6 desalting column (Biorad, Marnes-la-Coquette,
597 France). Samples were directly infused with nano-electrospray ionization with in-house-prepared
598 gold-coated borosilicate glass capillaries with a spray voltage of +1.4 kV. Spectra were recorded

599 on a quadrupole TOF instrument (Synapt G2 HDMS with 32K quadrupole, Waters) optimized for
600 transmission of native, high-m/z protein assemblies. Critical voltages and pressures throughout the
601 instrument were 50 V, 10 V, 150 V and 15 V for the sampling cone, extraction cone, trap and
602 transfer collision cell, respectively, with pressures of 9 mbar, 1.47×10^{-2} mbar and 1.21×10^{-2}
603 mbar for the source, trap and transfer regions unless indicated otherwise. CIU ion mobility
604 experiments were performed with 50 V sampling cone; 50-200 V trap collision energy; 42 V trap
605 DC bias; and 15 V transfer collision energy. Pressures throughout the instrument were 9 and 1.46
606 $\times 10^{-2}$ mbar for the source and trap/transfer collision cells. All spectra were processed with
607 Masslynx v4.1 (Waters). Collision cross section calibration was performed using GDH, ADH,
608 ConA and PK as proteins standard as described (Allen et al., 2016). It should be noted that due to
609 the generally lower charge states observed for membrane proteins, and the increased collision
610 energies required (compared to soluble proteins) for gentle release of proteins from detergent
611 micelles, the CCS values reported here are less accurate and intended for qualitative comparison
612 rather than quantitative matching to theoretical models.
613

614 **Peptide binding assays**

615 Synthesized peptides were dissolved in DMSO to a final concentration of 100 mM and added to
616 the protein sample at final concentrations of 10 μM FhaC and 100 μM peptide. To correct for non-
617 specific and detergent-specific binding, SphB1-αβ was run at identical concentrations and
618 conditions. For both proteins the fraction of peptide-bound protein was calculated based on peak
619 intensities, after which the binding to the decoy protein was subtracted to correct for non-specific
620 binding.
621

Acknowledgements

We thank Xavier Hanoulle for useful suggestions and discussions at the start of this project and Isabelle Landrieu for her support and advice. This work was funded by the Agence Nationale de Recherche grant ANR-17-CE11-0043-02 "OPEN_BAR" to FJD and a "Projets exploratoires premier soutien (PEPS)" grant by the CNRS and the University of Lille to RS. Financial support and spectrometer access by the IR-RMN-THC FR 3050 CNRS for conducting NMR experiments at the IR-RMN platforms in Lille and Grenoble is gratefully acknowledged. EPR experiments were performed within the national facility RENARD at the University of Lille (Federation IR-RPE 3443). Support by the Centre National de la Recherche Scientifique (CNRS), Université de Strasbourg (Unistra) and the French Proteomic Infrastructure (ProFI; ANR-10-INBS-08-03) is acknowledged. The authors would also like to thank the IdeX program of the University of Strasbourg for funding the Synapt G2Si instrument.

References

Allen, S. J., Eaton, R. M., & Bush, M. F. (2016). Analysis of native-like ions using structures for lossless ion manipulations. *Anal Chem, 88*(18), 9118-9126. https://doi.org/10.1021/acs.analchem.6b02089

Alsteens, D., Martinez, N., Jamin, M., & Jacob-Dubuisson, F. (2013). Sequential unfolding of Beta helical protein by single-molecule atomic force microscopy. *PLoS ONE, 8*(8), e73572. https://doi.org/10.1371/journal.pone.0073572

PONE-D-12-39879 [pii]

Alvira, S., Watkins, D. W., Troman, L., Allen, W. J., Lorriman, J. S., Degliesposti, G., Cohen, E. J., Beeby, M., Daum, B., Gold, V. A., Skehel, J. M., & Collinson, I. (2020). Inter-membrane association of the Sec and BAM translocons for bacterial outer-membrane biogenesis. *Elife, 9*. https://doi.org/10.7554/eLife.60669

Amero, C., Asuncion Dura, M., Noirclerc-Savoye, M., Perollier, A., Gallet, B., Plevin, M. J., Vernet, T., Franzetti, B., & Boisbouvier, J. (2011). A systematic mutagenesis-driven strategy for site-resolved NMR studies of supramolecular assemblies. *J Biomol NMR, 50*(3), 229-236. https://doi.org/10.1007/s10858-011-9513-5

Barbet-Massin, E., Pell, A. J., Retel, J. S., Andreas, L. B., Jaudzems, K., Franks, W. T., Nieuwkoop, A. J., Hiller, M., Higman, V., Guerry, P., Bertarello, A., Knight, M. J., Felletti, M., Le Marchand, T., Kotelovica, S., Akopjana, I., Tars, K., Stoppini, M., Bellotti, V., Bolognesi, M., Ricagno, S., Chou, J. J., Griffin, R. G., Oschkinat, H., Lesage, A., Emsley, L., Herrmann, T., & Pintacuda, G. (2014). Rapid proton-detected NMR assignment for proteins with fast magic angle spinning. *J Am Chem Soc, 136*(35), 12489-12497. https://doi.org/10.1021/ja507382j

Barrera, N. P., Isaacson, S. C., Zhou, M., Bavro, V. N., Welch, A., Schaedler, T. A., Seeger, M. A., Miguel, R. N., Korkhov, V. M., van Veen, H. W., Venter, H., Walmsley, A. R., Tate, C. G., & Robinson, C. V. (2009). Mass spectrometry of membrane transporters reveals subunit stoichiometry and interactions. *Nat Methods, 6*(8), 585-587. https://doi.org/10.1038/nmeth.1347

Battiste, J. L., & Wagner, G. (2000). Utilization of site-directed spin labeling and high-resolution heteronuclear nuclear magnetic resonance for global fold determination of large proteins with limited nuclear overhauser effect data. *Biochemistry, 39*(18), 5355-5365. https://doi.org/10.1021/bi000060h

Baud, C., Guerin, J., Petit, E., Lesne, E., Dupre, E., Locht, C., & Jacob-Dubuisson, F. (2014). Translocation path of a substrate protein through its Omp85 transporter. *Nat Commun, 5*, 5271. https://doi.org/10.1038/ncomms6271

Bayburt, T. H., Carlson, J. W., & Sligar, S. G. (1998). Reconstitution and imaging of a membrane protein in a nanometer-size phospholipid bilayer. *J Struct Biol, 123*(1), 37-44. https://doi.org/10.1006/jsbi.1998.4007

Bennett, A. E., Griffin, R. G., Ok, J. H., & Vega, S. (1992). Chemical shift correlation spectroscopy in rotating solids: Radio frequency-driven dipolar recoupling and longitudinal exchange. *J. Chem. Phys., 96*, 8624–8627.

Bertini, I., Engelke, F., Gonnelli, L., Knott, B., Luchinat, C., Osen, D., & Ravera, E. (2012). On the use of ultracentrifugal devices for sedimented solute NMR. *J Biomol NMR, 54*(2), 123-127. https://doi.org/10.1007/s10858-012-9657-y

Clantin, B., Delattre, A. S., Rucktooa, P., Saint, N., Meli, A. C., Locht, C., Jacob-Dubuisson, F., & Villeret, V. (2007). Structure of the membrane protein FhaC: a member of the Omp85-TpsB transporter superfamily. *Science, 317*(5840), 957-961. https://doi.org/10.1126/science.1143860

Clore, G. M., & Iwahara, J. (2009). Theory, practice, and applications of paramagnetic relaxation enhancement for the characterization of transient low-population states of biological macromolecules and their complexes. *Chem Rev, 109*(9), 4108-4139. https://doi.org/10.1021/cr900033p

Dé, E., Saint, N., Glinel, K., Méli, A. C., Levy, D., & Jacob-Dubuisson, F. (2008). Influence of the passenger domain of a model autotransporter on the properties of its translocator domain. *Mol Membr Biol, 25*(3), 192-202. https://doi.org/10.1080/09687680701771925

Delaglio, F., Grzesiek, S., Vuister, G. W., Zhu, G., Pfeifer, J., & Bax, A. (1995). NMRPipe: a multidimensional spectral processing system based on UNIX pipes. *J Biomol NMR, 6*(3), 277-293. https://doi.org/10.1007/BF00197809

Delattre, A. S., Clantin, B., Saint, N., Locht, C., Villeret, V., & Jacob-Dubuisson, F. (2010, Nov). Functional importance of a conserved sequence motif in FhaC, a prototypic member of the TpsB/Omp85 superfamily. *FEBS J, 277*(22), 4755-4765. https://doi.org/10.1111/j.1742-4658.2010.07881.x

Delattre, A. S., Saint, N., Clantin, B., Willery, E., Lippens, G., Locht, C., Villeret, V., & Jacob-Dubuisson, F. (2011). Substrate recognition by the POTRA domains of TpsB transporter FhaC. *Mol Microbiol, 81*(1), 99-112. https://doi.org/10.1111/j.1365-2958.2011.07680.x

Derbise, A., Lesic, B., Dacheux, D., Ghigo, J.-M., & Carniel, E. (2003). A rapid and simple method for inactivating chromosomal genes in *Yersinia*. *FEMS Immunol Med Microbiol, 38*, 113-116. https://doi.org/10.1016/S0928-8244(03)00181-0

Diederichs, K. A., Ni, X., Rollauer, S. E., Botos, I., Tan, X., King, M. S., Kunji, E. R. S., Jiang, J., & Buchanan, S. K. (2020). Structural insight into mitochondrial beta-barrel outer membrane protein biogenesis. *Nat Commun, 11*(1), 3290. https://doi.org/10.1038/s41467-020-17144-1

Doerner, P. A., & Sousa, M. C. (2017). Extreme Dynamics in the BamA beta-Barrel Seam. *Biochemistry, 56*(24), 3142-3149. https://doi.org/10.1021/acs.biochem.7b00281

Doyle, M. T., & Bernstein, H. D. (2019). Bacterial outer membrane proteins assemble via asymmetric interactions with the BamA beta-barrel. *Nat Commun, 10*(1), 3358. https://doi.org/10.1038/s41467-019-11230-9

Estrada Mallarino, L., Fan, E., Odermatt, M., Muller, M., Lin, M., Liang, J., Heinzelmann, M., Fritsche, F., Apell, H. J., & Welte, W. (2015). TtOmp85, a beta-barrel assembly protein, functions by barrel augmentation. *Biochemistry, 54*(3), 844-852. https://doi.org/10.1021/bi5011305

Fan, E., Fiedler, S., Jacob-Dubuisson, F., & Muller, M. (2012). Two-partner secretion of gram-negative bacteria: a single beta-barrel protein enables transport across the outer membrane. *J Biol Chem, 287*(4), 2591-2599. https://doi.org/10.1074/jbc.M111.293068

735 Gu, Y., Li, H., Dong, H., Zeng, Y., Zhang, Z., Paterson, N. G., Stansfeld, P. J., Wang, Z., Zhang, Y., Wang, W.,
736 & Dong, C. (2016). Structural basis of outer membrane protein insertion by the BAM complex.
737 *Nature, 531*(7592), 64-69. https://doi.org/10.1038/nature17199

738

739 Guedin, S., Willery, E., Locht, C., & Jacob-Dubuisson, F. (1998). Evidence that a globular conformation is
740 not compatible with FhaC-mediated secretion of the Bordetella pertussis filamentous
741 haemagglutinin. *Mol Microbiol, 29*(3), 763-774. https://doi.org/10.1046/j.1365-
742 2958.1998.00970.x

743

744 Guedin, S., Willery, E., Tommassen, J., Fort, E., Drobecq, H., Locht, C., & Jacob-Dubuisson, F. (2000). Novel
745 topological features of FhaC, the outer membrane transporter involved in the secretion of the
746 *Bordetella pertussis* filamentous hemagglutinin. *J Biol Chem, 275*(39), 30202-30210.
747 https://doi.org/10.1074/jbc.M005515200

748

749 Guerin, J., Baud, C., Touati, N., Saint, N., Willery, E., Locht, C., Vezin, H., & Jacob-Dubuisson, F. (2014).
750 Conformational dynamics of protein transporter FhaC: large-scale motions of plug helix. *Mol*
751 *Microbiol, 92*(6), 1164-1176. https://doi.org/10.1111/mmi.12585

752

753 Guerin, J., Bigot, S., Schneider, R., Buchanan, S. K., & Jacob-Dubuisson, F. (2017). Two-partner secretion:
754 Combining efficiency and simplicity in the secretion of large proteins for bacteria-host and
755 bacteria-bacteria interactions. *Front Cell Infect Microbiol, 7*, 148.
756 https://doi.org/10.3389/fcimb.2017.00148

757

758 Guerin, J., Botos, I., Zhang, Z., Lundquist, K., Gumbart, J. C., & Buchanan, S. K. (2020). Structural insight
759 into toxin secretion by contact-dependent growth inhibition transporters. *Elife, 9*.
760 https://doi.org/10.7554/eLife.58100

761

762 Guerin, J., Saint, N., Baud, C., Meli, A. C., Etienne, E., Locht, C., Vezin, H., & Jacob-Dubuisson, F. (2015).
763 Dynamic interplay of membrane-proximal POTRA domain and conserved loop L6 in Omp85
764 transporter FhaC. *Mol Microbiol, 98*(3), 490-501. https://doi.org/10.1111/mmi.13137

765

766 Hagelueken, G., Abdullin, D., & Schiemann, O. (2015). mtsslSuite: Probing biomolecular conformation by
767 spin-labeling studies. *Methods Enzymol, 563*, 595-622.
768 https://doi.org/10.1016/bs.mie.2015.06.006

769

770 Hagelueken, G., Ward, R., Naismith, J. H., & Schiemann, O. (2012, Apr). MtsslWizard: In Silico Spin-Labeling
771 and Generation of Distance Distributions in PyMOL. *Appl Magn Reson, 42*(3), 377-391.
772 https://doi.org/10.1007/s00723-012-0314-0

773

774 Halladin, D. K., Ortega, F. E., Ng, K. M., Footer, M. J., Mitic, N. S., Malkov, S. N., Gopinathan, A., Huang, K.
775 C., & Theriot, J. A. (2021, Aug). Entropy-driven translocation of disordered proteins through the

Gram-positive bacterial cell wall. *Nat Microbiol, 6*(8), 1055-1065. https://doi.org/10.1038/s41564-021-00942-8

Hartmann, J. B., Zahn, M., Burmann, I. M., Bibow, S., & Hiller, S. (2018). Sequence-specific solution NMR assignments of the beta-barrel insertase BamA to monitor its conformational ensemble at the atomic level. *J Am Chem Soc, 140*(36), 11252-11260. https://doi.org/10.1021/jacs.8b03220

Heinz, E., & Lithgow, T. (2014). A comprehensive analysis of the Omp85/TpsB protein superfamily structural diversity, taxonomic occurrence, and evolution. *Front Microbiol, 5*, 370. https://doi.org/10.3389/fmicb.2014.00370

Höhr, A. I. C., Lindau, C., Wirth, C., Qiu, J., Stroud, D. A., Kutik, S., Guiard, B., Hunte, C., Becker, T., Pfanner, N., & Wiedemann, N. (2018). Membrane protein insertion through a mitochondrial beta-barrel gate. *Science, 359*(6373). https://doi.org/10.1126/science.aah6834

Iadanza, M. G., Higgins, A. J., Schiffrin, B., Calabrese, A. N., Brockwell, D. J., Ashcroft, A. E., Radford, S. E., & Ranson, N. A. (2016). Lateral opening in the intact beta-barrel assembly machinery captured by cryo-EM. *Nat Commun, 7*, 12865. https://doi.org/10.1038/ncomms12865

Iadanza, M. G., Schiffrin, B., White, P., Watson, M. A., Horne, J. E., Higgins, A. J., Calabrese, A. N., Brockwell, D. J., Tuma, R., Kalli, A. C., Radford, S. E., & Ranson, N. A. (2020). Distortion of the bilayer and dynamics of the BAM complex in lipid nanodiscs. *Commun Biol, 3*(1), 766. https://doi.org/10.1038/s42003-020-01419-w

Iwahara, J., Tang, C., & Marius Clore, G. (2007). Practical aspects of (1)H transverse paramagnetic relaxation enhancement measurements on macromolecules. *J Magn Reson, 184*(2), 185-195. https://doi.org/10.1016/j.jmr.2006.10.003

Jeschke, G. (2012). DEER distance measurements on proteins. *Annu Rev Phys Chem, 63*, 419-446. https://doi.org/10.1146/annurev-physchem-032511-143716

Jeschke, G. (2013). Conformational dynamics and distribution of nitroxide spin labels. *Prog Nucl Magn Reson Spectrosc, 72*, 42-60. https://doi.org/10.1016/j.pnmrs.2013.03.001

Jeschke, G. (2020). MMM: Integrative ensemble modeling and ensemble analysis. *Protein Sci*. https://doi.org/10.1002/pro.3965

Jeschke, G., Chechik, V., Ionita, P., Godt, A., Zimmermann, H., Banham, J., Timmel, C. R., Hilger, D., & Jung, H. (2006). DeerAnalysis – a comprehensive software package for analyzing pulsed ELDOR data 2006, 30, 473-498. *Appl Magnetic Reson, 30*, 473-498.

817 Knowles, T. J., Scott-Tucker, A., Overduin, M., & Henderson, I. R. (2009). Membrane protein architects:
818 the role of the BAM complex in outer membrane protein assembly. *Nat Rev Microbiol, 7*(3), 206-
819 214. https://doi.org/10.1038/nrmicro2069

820

821 Kurauskas, V., Weber, E., Hessel, A., Ayala, I., Marion, D., & Schanda, P. (2016). Cross-correlated relaxation
822 of dipolar coupling and chemical-shift anisotropy in magic-angle spinning R1rho NMR
823 measurements: Application to protein backbone dynamics measurements. *J Phys Chem B, 120*(34),
824 8905-8913. https://doi.org/10.1021/acs.jpcb.6b06129

825

826 Landreh, M., Marty, M., Gault, J., & Robinson, C. (2016). A sliding selectivity scale for lipid binding to
827 membrane proteins *Curr Op Struct Biol, 39*, 54-60. https://doi.org/10.1016/j.sbi.2016.04.005

828

829 Lee, W., Tonelli, M., & Markley, J. L. (2015). NMRFAM-SPARKY: enhanced software for biomolecular NMR
830 spectroscopy. *Bioinformatics, 31*(8), 1325-1327. https://doi.org/10.1093/bioinformatics/btu830

831

832 Lewandowski, J. R., Sass, H. J., Grzesiek, S., Blackledge, M., & Emsley, L. (2011). Site-specific measurement
833 of slow motions in proteins. *J Am Chem Soc, 133*(42), 16762-16765.
834 https://doi.org/10.1021/ja206815h

835

836 Liang, B., & Tamm, L. K. (2016). NMR as a tool to investigate the structure, dynamics and function of
837 membrane proteins. *Nat Struct Mol Biol, 23*(6), 468-474. https://doi.org/10.1038/nsmb.3226

838

839 Ma, P., Haller, J. D., Zajakala, J., Macek, P., Sivertsen, A. C., Willbold, D., Boisbouvier, J., & Schanda, P.
840 (2014). Probing transient conformational states of proteins by solid-state R(1rho) relaxation-
841 dispersion NMR spectroscopy. *Angew Chem Int Ed Engl, 53*(17), 4312-4317.
842 https://doi.org/10.1002/anie.201311275

843

844 Maier, T., Clantin, B., Gruss, F., Dewitte, F., Delattre, A. S., Jacob-Dubuisson, F., Hiller, S., & Villeret, V.
845 (2015). Conserved Omp85 lid-lock structure and substrate recognition in FhaC. *Nat Commun, 6*,
846 7452. https://doi.org/10.1038/ncomms8452

847

848 Méli, A. C., Hodak, H., Clantin, B., Locht, C., Molle, G., Jacob-Dubuisson, F., & Saint, N. (2006). Channel
849 properties of TpsB transporter FhaC point to two functional domains with a C-terminal protein-
850 conducting pore. *J Biol Chem, 281*, 158-166. https://doi.org/10.1074/jbc.M508524200

851

852 Mittermaier, A. K., & Kay, L. E. (2009). Observing biological dynamics at atomic resolution using NMR.
853 *Trends Biochem Sci, 34*(12), 601-611. https://doi.org/10.1016/j.tibs.2009.07.004

854

855 Nadaud, P. S., Helmus, J. J., Hofer, N., & Jaroniec, C. P. (2007). Long-range structural restraints in spin-
856 labeled proteins probed by solid-state nuclear magnetic resonance spectroscopy. *J Am Chem Soc,*
857 *129*(24), 7502-7503. https://doi.org/10.1021/ja072349t

Nash, Z. M., & Cotter, P. A. (2019). Bordetella filamentous hemagglutinin, a model for the Two-Partner Secretion pathway. *Microbiol Spectrum, 2*(7), 10.1128. https://doi.org/10.1128/microbiolspec.PSIB-0024-2018

Noinaj, N., Gumbart, J. C., & Buchanan, S. K. (2017). The beta-barrel assembly machinery in motion. *Nat Rev Microbiol, 15*(4), 197-204. https://doi.org/10.1038/nrmicro.2016.191

Noinaj, N., Kuszak, A. J., Balusek, C., Gumbart, J. C., & Buchanan, S. K. (2014). Lateral opening and exit pore formation are required for BamA function. *Structure, 22*(7), 1055-1062. https://doi.org/10.1016/j.str.2014.05.008

Noinaj, N., Kuszak, A. J., Gumbart, J. C., Lukacik, P., Chang, H., Easley, N. C., Lithgow, T., & Buchanan, S. K. (2013). Structural insight into the biogenesis of beta-barrel membrane proteins. *Nature, 501*(7467), 385-390. https://doi.org/10.1038/nature12521

Palmer, A. G., 3rd, & Massi, F. (2006). Characterization of the dynamics of biomacromolecules using rotating-frame spin relaxation NMR spectroscopy. *Chem Rev, 106*(5), 1700-1719. https://doi.org/10.1021/cr0404287

Pannier, M., Veit, S., Godt, A., Jeschke, G., & Spiess, H. W. (2000). Dead-time free measurement of dipole-dipole interactions between electron spins. *J Magnetic Reson 142*, 331-340.

Peterson, J. H., Tian, P., Ieva, R., Dautin, N., & Bernstein, H. D. (2010, Oct 12). Secretion of a bacterial virulence factor is driven by the folding of a C-terminal segment. *Proc Natl Acad Sci U S A, 107*(41), 17739-17744. https://doi.org/10.1073/pnas.1009491107

Renault, M., Bos, M. P., Tommassen, J., & Baldus, M. (2011). Solid-state NMR on a large multidomain integral membrane protein: the outer membrane protein assembly factor BamA. *J Am Chem Soc, 133*(12), 4175-4177. https://doi.org/10.1021/ja109469c

Ritchie, T. K., Grinkova, Y. V., Bayburt, T. H., Denisov, I. G., Zolnerciks, J. K., Atkins, W. M., & Sligar, S. G. (2009). Reconstitution of membrane proteins in phospholipid bilayer nanodiscs. *Methods Enzymol, 464*, 211-231. https://doi.org/10.1016/S0076-6879(09)64011-8

Ruschak, A. M., & Kay, L. E. (2010). Methyl groups as probes of supra-molecular structure, dynamics and function. *J Biomol NMR, 46*(1), 75-87. https://doi.org/10.1007/s10858-009-9376-1

Sahu, I. D., & Lorigan, G. A. (2020). Electron paramagnetic resonance as a tool for studying membrane proteins. *Biomolecules, 10*(5). https://doi.org/10.3390/biom10050763

Schanda, P., & Brutscher, B. (2005). Very fast two-dimensional NMR spectroscopy for real-time investigation of dynamic events in proteins on the time scale of seconds. *J Am Chem Soc, 127*(22), 8014-8015. https://doi.org/10.1021/ja051306e

Tian, Y., Han, L., Buckner, A. C., & Ruotolo, B. T. (2015). Collision induced unfolding of intact antibodies: Rapid characterization of disulfide bonding patterns, glycosylation, and structures. *Anal Chem, 87*(22), 11509-11515. https://doi.org/10.1021/acs.analchem.5b03291

Tomasek, D., Rawson, S., Lee, J., Wzorek, J. S., Harrison, S. C., Li, Z., & Kahne, D. (2020). Structure of a nascent membrane protein as it folds on the BAM complex. *Nature, 583*(7816), 473-478. https://doi.org/10.1038/s41586-020-2370-1

Torricella, F., Pierro, A., Mileo, E., Belle, V., & Bonucci, A. (2021). Nitroxide spin labels and EPR spectroscopy: A powerful association for protein dynamics studies. *Biochim Biophys Acta Proteins Proteom, 1869*(7), 140653. https://doi.org/10.1016/j.bbapap.2021.140653

Venditti, V., Fawzi, N. L., & Clore, G. M. (2011). Automated sequence- and stereo-specific assignment of methyl-labeled proteins by paramagnetic relaxation and methyl-methyl nuclear Overhauser enhancement spectroscopy. *J Biomol NMR, 51*(3), 319-328. https://doi.org/10.1007/s10858-011-9559-4

Viegas, A., Viennet, T., & Etzkorn, M. (2016). The power, pitfalls and potential of the nanodisc system for NMR-based studies. *Biol Chem, 397*(12), 1335-1354. https://doi.org/10.1515/hsz-2016-0224

Vranken, W. F., Boucher, W., Stevens, T. J., Fogh, R. H., Pajon, A., Llinas, M., Ulrich, E. L., Markley, J. L., Ionides, J., & Laue, E. D. (2005). The CCPN data model for NMR spectroscopy: development of a software pipeline. *Proteins, 59*(4), 687-696. https://doi.org/10.1002/prot.20449

Warner, L. R., Gatzeva-Topalova, P. Z., Doerner, P. A., Pardi, A., & Sousa, M. C. (2017). Flexibility in the periplasmic domain of BamA is important for function. *Structure, 25*(1), 94-106. https://doi.org/10.1016/j.str.2016.11.013

Wu, R., Bakelar, J. W., Lundquist, K., Zhang, Z., Kuo, K. M., Ryoo, D., Pang, Y. T., Sun, C., White, T., Klose, T., Jiang, W., Gumbart, J. C., & Noinaj, N. (2021, Dec 8). Plasticity within the barrel domain of BamA mediates a hybrid-barrel mechanism by BAM. *Nat Commun, 12*(1), 7131. https://doi.org/10.1038/s41467-021-27449-4

Xiao, L., Han, L., Li, B., Zhang, M., Zhou, H., Luo, Q., Zhang, X., & Huang, Y. (2021). Structures of the beta-barrel assembly machine recognizing outer membrane protein substrates. *FASEB J, 35*(1), e21207. https://doi.org/10.1096/fj.202001443RR

Zhong, Y., Han, L., & Ruotolo, B. (2014). Collisional and coulombic unfolding of gas-phase proteins: High correlation to their domain structures in solution *Angew. Chem, 53*(35), 9209-9212. https://doi.org/10.1002/anie.201403784

Zhou, D. H., & Rienstra, C. M. (2008). High-performance solvent suppression for proton detected solid-state NMR. *J Magn Reson, 192*(1), 167-172. https://doi.org/10.1016/j.jmr.2008.01.012

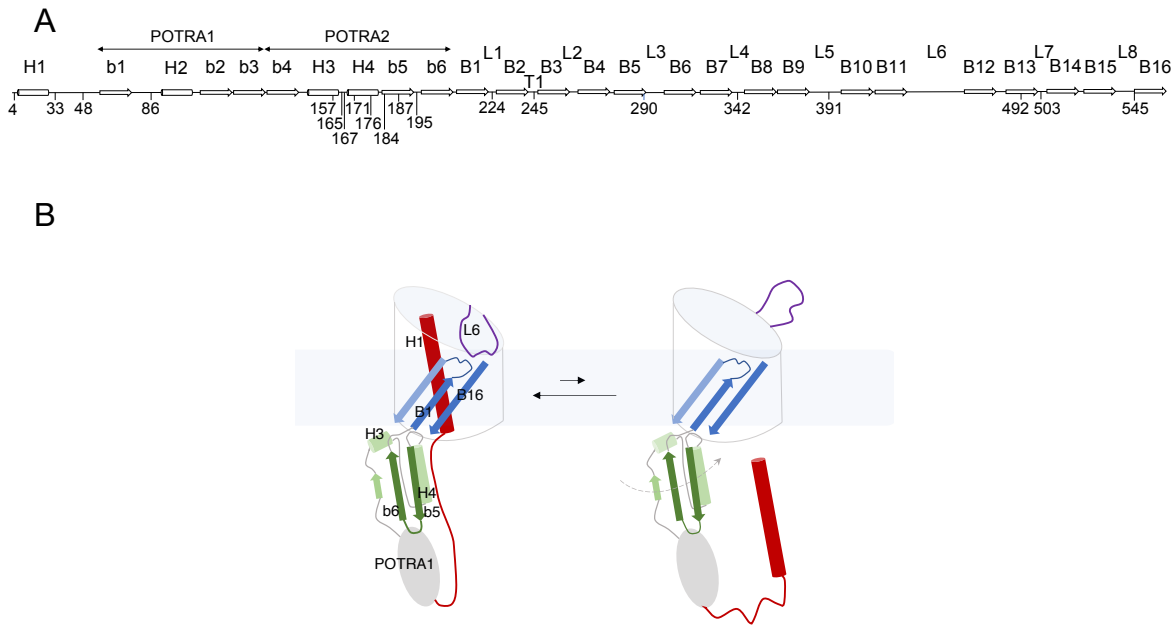

Figure 1. FhaC: Secondary structure and intrinsic dynamics. (A) Linear representation of the secondary structure elements of FhaC, with residues used in this work. L1 to L8 represent the extracellular loops, b1 to b6 the β strands of the POTRA domains, H1 to H4 the α helices, and B1 to B16 the β-barrel strands. T1 is the first periplasmic turn. (B) Schematic representation of known FhaC motions linked to its activity. Specific structural elements are colored as follows: H1 and the linker in red, the POTRA2 domain in shades of green, L6 in purple, and β barrel strands B1, B2 and B16 in shades of blue. In its resting conformation (left), FhaC is closed, with H1 crossing the β barrel. The linker is positioned along the H4 helix of the POTRA2 domain (Maier et al., 2015), thus obstructing a major substrate binding site (Delattre et al., 2011). L6 is folded inside the barrel with a conserved interaction between its tip and the barrel wall. This conformation is in equilibrium with an open form (right), in which H1 has vacated the pore and the substrate binding site is available (Guerin et al., 2014). We have obtained evidence that L6 also moves away from its resting position in the β barrel and that the POTRA2 domain undergoes so far undefined motions (represented as a dashed line) (Guerin et al., 2015).

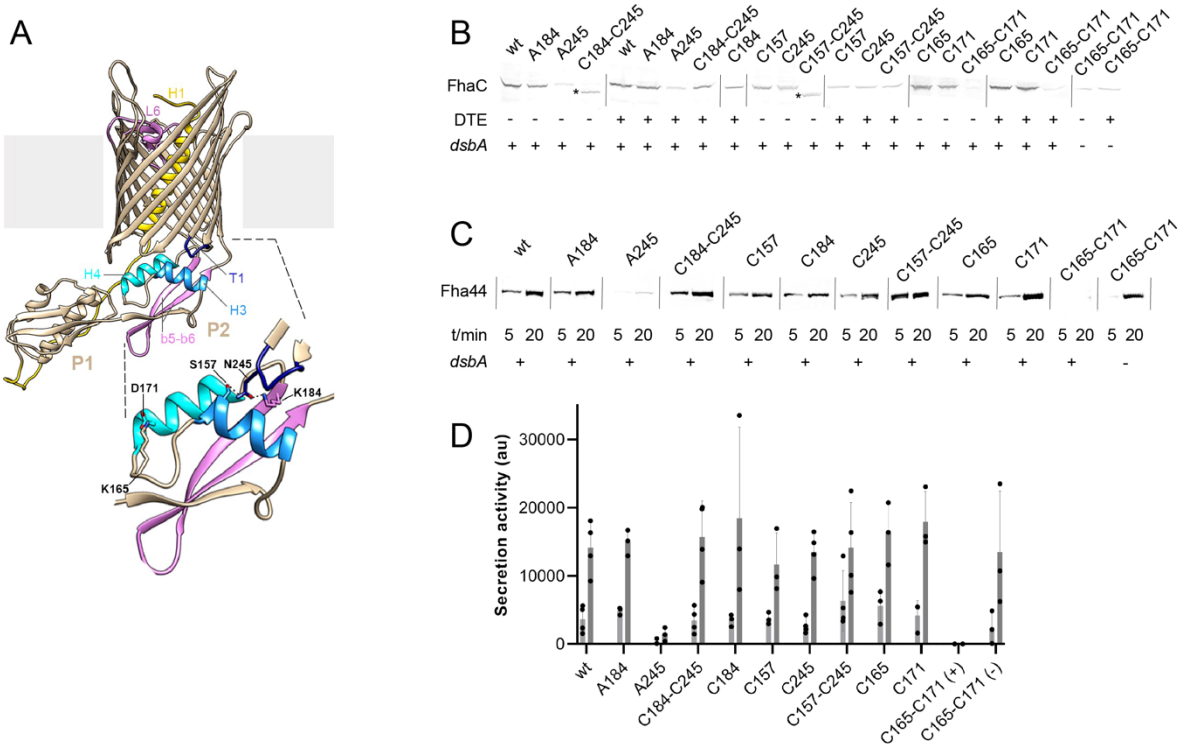

Figure 2. Effects of engineered S-S bonds on FhaC activity. (A) Structural model of FhaC (PDB 4QKY). A zoom of the POTRA2 domain is shown below. (B) Residues involved in a salt bridge (Lys^{165}-Asp^{171}) or H bonds (Lys^{184}-Asn^{245}; Ser^{157}-Asn^{245}) in the resting conformation of FhaC were replaced as indicated (C=Cys; A=Ala). Immunoblots were performed on membrane extracts with anti-FhaC antibodies. The asterisks indicate oxidized species of FhaC detected in the absence of the reducing agent dithioerythritol (DTE) in the sample buffer. (C) The secretion activity of the FhaC variants was determined using a model substrate, Fha44-His, affinity precipitated from supernatants 5 and 20 min after induction. Immunoblots were developed with an anti-6His tag monoclonal antibody. (D) Quantification of Fha44 found in culture supernatants after 5 and 20 min. The means and standard deviations of the means are shown (n=3 or 4). Activity of $FhaC^{C165+C171}$ could only be detected in the *dsbA* KO strain (denoted C165-C171(-)), not in its wild type parent (denoted C165-C171(+)).

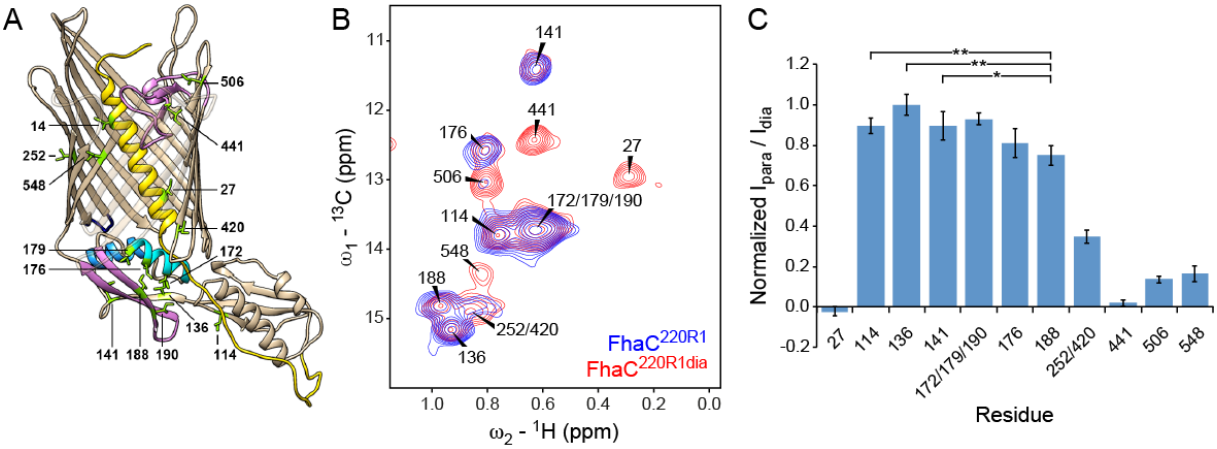

Figure 3. NMR analysis of Ile δ_1-methyl labeled FhaC in lipid bilayers. (A) Structure of FhaC with Ile residues labeled and drawn as green sticks. Color code of structural elements is as in Fig. 1. β-strands 1 to 4 are drawn transparently for visibility. (B) Superposition of the methyl regions of solid-state dipolar hCH ^{13}C-^{1}H correlation spectra of u-(^{2}H, ^{15}N), Ile-δ_1($^{13}CH_3$)-labeled FhaC samples in *E. coli* polar lipid liposomes, with a paramagnetic MTSL tag ($FhaC^{220R1}$, blue) or with a diamagnetic MTSL analog ($FhaC^{220R1dia}$, red) attached to the introduced Cys^{220} residue. Spectra were recorded at 800 MHz ^{1}H Larmor frequency and 50 kHz MAS. (C) Ratios I_{para}/I_{dia} of Ile-δ1 methyl peak intensities in the hCH correlation spectra of $FhaC^{220R1}$ and $FhaC^{220R1dia}$ shown in (B), normalized to the maximum ratio observed in Ile^{136}. Error bars are calculated based on spectral noise levels. * and ** indicate significant ($p < 0.05$ and $p < 0.01$, respectively) attenuation of the Ile^{188} signal relative to the signals of the reference residues Ile^{114}, Ile^{136}, and Ile^{141}. These analyses were complemented by analyses of scalar coupling-based spectra in liposomes and nanodiscs (Supplement 1), through-space correlations (Supplement 2), and relaxation dispersion experiments (Supplement 3). Estimated distances between MTSL probe and Ile residues in $FhaC^{220R1}$ as expected from the crystal structure are shown in Supplement 4.

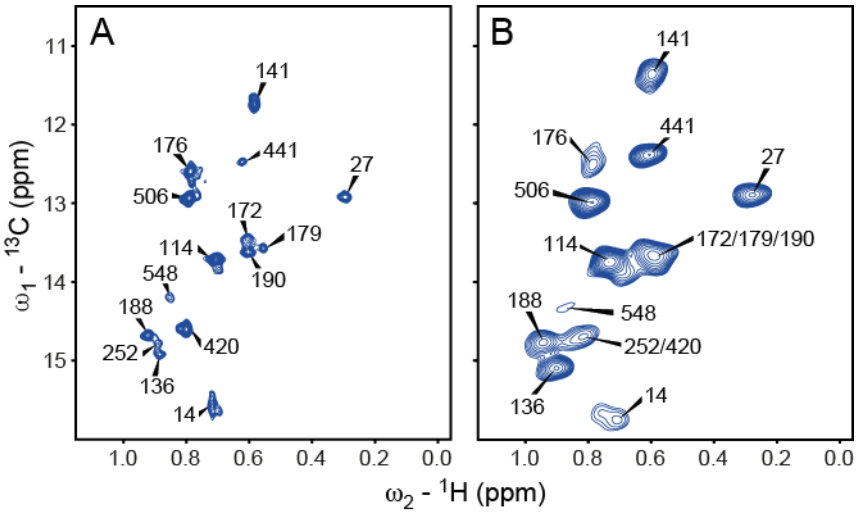

Figure 3 Supplement 1. NMR analyses of Ile δ_1 methyl labeled FhaC in lipid bilayers. (A) Methyl region of a solution-state heteronuclear multiple quantum coherence (HMQC) ^{13}C-^{1}H correlation spectrum of u-(^{2}H, ^{15}N), Ile-δ_1($^{13}CH_3$)-labeled FhaC^{195R1} in ^{2}H-MSP1D1 nanodiscs prepared from deuterated (d_{54}-) DMPC and DMPG (2:1) lipids, recorded on a 900 MHz spectrometer. The MTSL tag on residue 195 was reduced with ascorbic acid; peak positions are identical to those of wt FhaC in nanodiscs. (B) Same region of a scalar coupling-based solid-state J-HSQC ^{13}C-^{1}H correlation spectrum of wt FhaC (same isotope labeling as in (A)) in d_{54}-DMPC/DMPG liposomes, recorded on an 800 MHz spectrometer at 50 kHz MAS.

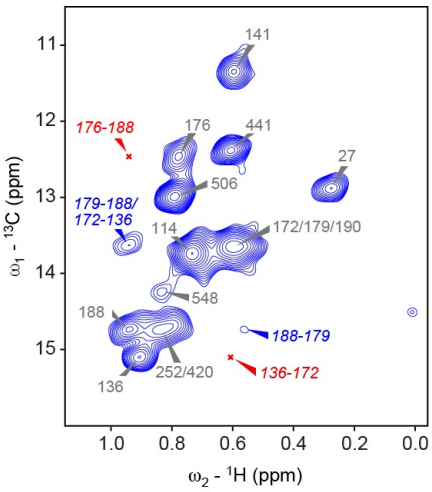

Figure 3 Supplement 2. NMR analysis of through-space contacts between Ile δ_1 methyl groups in FhaC in liposomes. 2D hChH correlation spectrum with 6.4 ms RFDR (Bennett et al., 1992) ^{1}H-^{1}H mixing of FhaC u-(^{2}H, ^{15}N), Ile-δ_1($^{13}CH_3$) in deuterated (d_{54}-) DMPC/ DMPG liposomes, recorded on an 800 MHz NMR spectrometer at 50 kHz MAS, to visualize through-space correlations between Ile δ_1 methyl groups close in space. Among expected inter-residue cross-peaks (^{1}H-^{1}H distance below 6 Å), peaks present in the spectrum are indicated in blue, those which are absent in red.

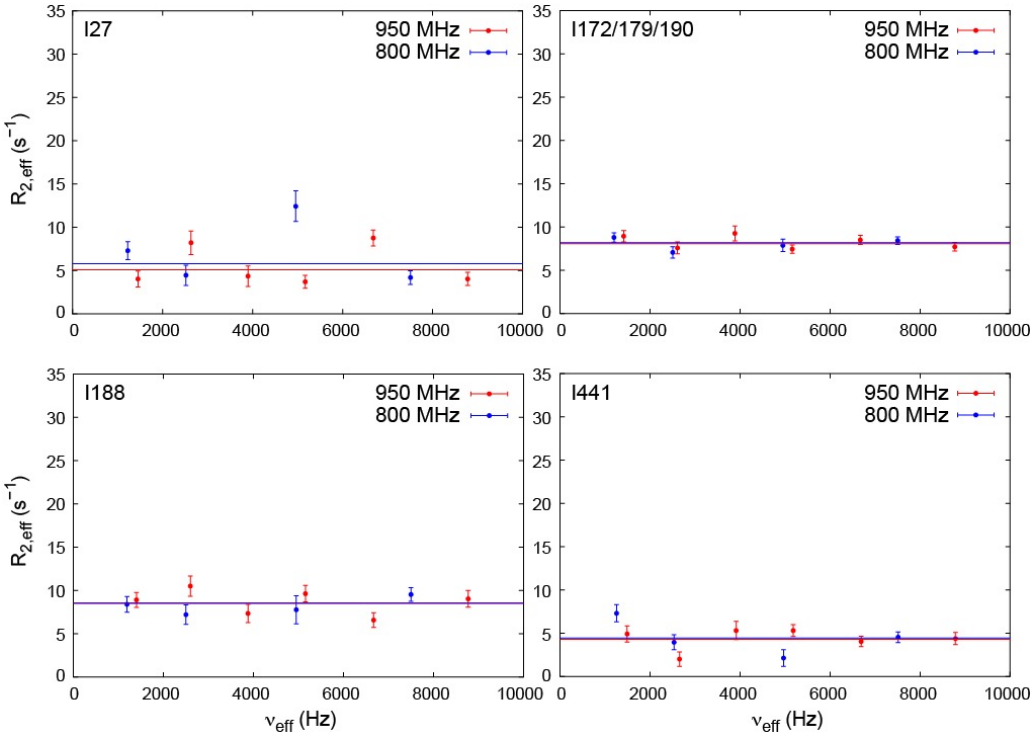

Figure 3 Supplement 3. NMR relaxation dispersion experiments to measure µs time scale exchange dynamics in FhaC. Effective ^{13}C transverse relaxation rates $R_{2,eff}$ extracted from solid-state NMR $R_{1\rho}$ relaxation dispersion experiments (Lewandowski et al., 2011; Ma et al., 2014) on selected Ile-δ_1 methyl groups of u-(^{2}H, ^{15}N), Ile-δ_1($^{13}CH_3$)-labeled wt FhaC, recorded on 800 (blue) and 950 MHz (red) spectrometers at 50 kHz MAS frequency and 17°C sample temperature. Horizontal lines are best fits to the data using a model of no exchange (i.e. constant $R_{2,eff}$ values for varying applied B_1 radiofrequency fields and thus varying effective fields ν_{eff}). Models assuming exchange do not fit the data significantly better according to F test statistics or Akaike's information criterion (AIC) in any of the Ile-δ_1($^{13}CH_3$) groups of FhaC. Notably, data from residue Ile^{548} in strand β16, at the barrel junction with strand β1, could not be reliably analyzed due to low signal-to-noise.

Ile residue	Avg. dist. to paramag. center (Å)
14	7.1
252	11.7
548	16.5
27	17.5
441	18.6
506	25.3
420	32.0
179	32.1
176	34.1
188	35.4
141	38.4
172	40.4
136	42.0
190	43.5
114	56.6

Figure 3 Supplement 4. Estimated Ile $C\delta_1$ – MTSL distances in the crystal structure conformation of $FhaC^{220R1}$. Shown are distances (in Å) between Ile $C\delta_1$ nuclei and the estimated average position of the paramagnetic center in FhaC with a MTSL spin label on residue 220 ($FhaC^{220R1}$). An ensemble of 200 MTSL conformations compatible with labeling on FhaC residue 220 was calculated using the mtsslSuite web server (Hagelueken et al., 2012; Hagelueken et al., 2015) (http://www.mtsslsuite.isb.ukbonn.de/) and the FhaC crystal structure (PDB 4QKY). The average position of the paramagnetic center (taken as halfway between nitrogen and oxygen atoms of the MTSL nitroxide ring) was calculated from the coordinates of these 200 conformations; distances from that position to Ile $C\delta_1$ nuclei were calculated using PyMOL (The PyMOL Molecular Graphics System. Schrödinger, LLC). A horizontal line in the table indicates the distance from the paramagnetic center up to which attenuation effects on the NMR resonance of the corresponding Ile residue are expected if FhaC assumes a conformation as in the crystal structure.

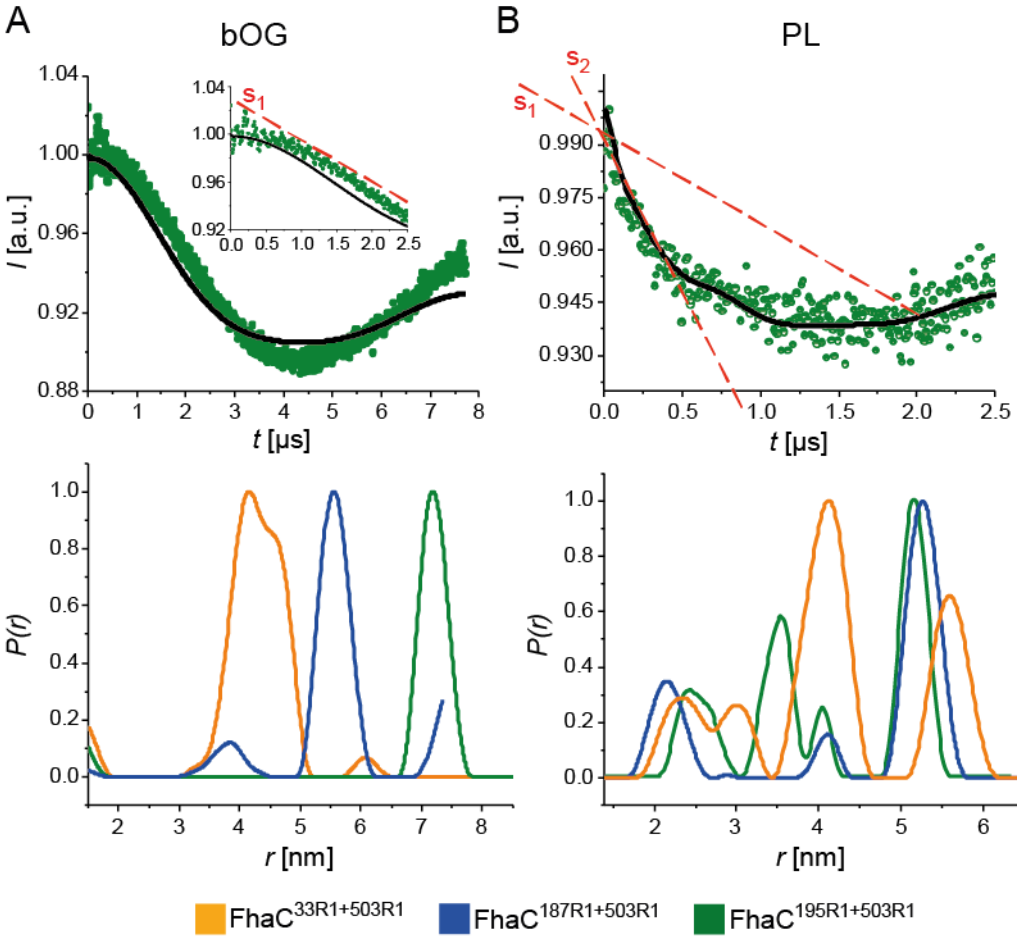

Figure 4. **PELDOR analyses of FhaC**. Dipolar evolution function for FhaC$^{195R1+503R1}$ (top), and distance distributions obtained by Tikhonov regularization of the dipolar evolution functions (bottom) for FhaC$^{33R1+503R1}$(orange), FhaC$^{187R1+503R1}$ (blue), and FhaC$^{195R1+503R1}$ (green) in bOG (A) and in proteoliposomes (B) prepared with *E. coli* polar lipids (PL). The black lines in the upper panels correspond to the fitting of the experimental PELDOR traces. The inset in A represents the first 2.5 µs of the dipolar evolution function for comparison with that shown in (B). The red dashed lines denoted S1 and S2 show the slopes of the first parts of the curves representing the dipolar evolution functions. Predicted distance distributions can be found in Supplement 1. Note that the longest distances measured depend on the dipolar evolution time *t*. As the lipid environment decreases the *t* that can be applied, the longest distances shift to smaller values for FhaC in proteoliposomes compared to bOG (Supplement 2). A mutation that severs the connection of the loop L6 to the inner barrel wall affects the EPR spectra of FhaC$^{195R1+503R1}$ (Supplement 3). Spectroscopic analyses (PELDOR EPR and PRE NMR) of FhaC in nanodiscs complement these data (Supplement 4).

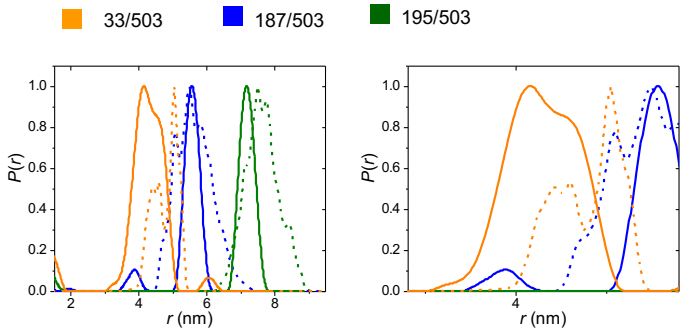

Figure 4 Supplement 1. Distance distributions from PELDOR experiments. The distance distributions obtained for FhaC$^{33R1+503R1}$ (orange), FhaC$^{187R1+503R1}$ (blue) and FhaC$^{195R1+503R1}$ (green) in bOG (solid lines) are compared with those predicted using a pre-computed rotamer library of the MTSL spin probe attached to specific residues on the PDB structure of FhaC (dashed lines) (Jeschke, 2020). In the right panel, a zoom on the 3-5 nm region shows the broad distribution for FhaC$^{33R1+503R1}$.

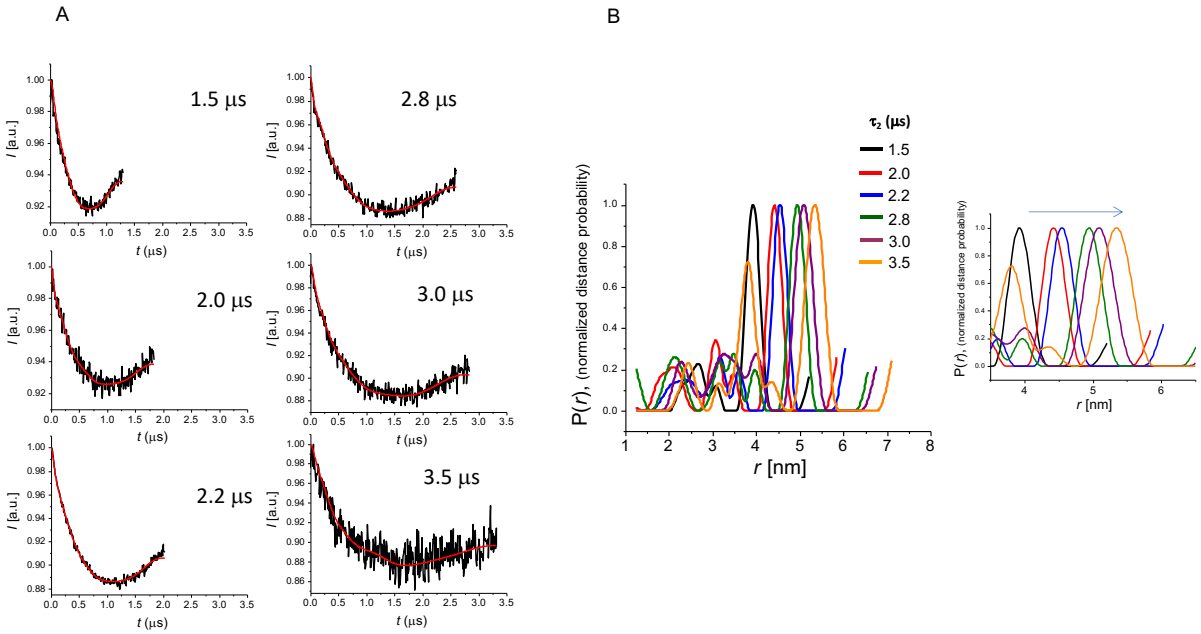

Figure 4 Supplement 2. Dipolar evolution signals recorded with different delays τ_2 and corresponding distance distributions. FhaC$^{195R1+503R1}$ in *E. coli* lipids liposomes was used in this experiment. (A) The dipolar evolution signals were measured at increasing dipolar evolution times *t*. (B) The longest distance measured shifts to longer values for longer dipolar evolution times *t* since long, but not short distances are sensitive to the value used in PELDOR experiments. The lipid environment decreases the dipolar evolution time that can be applied, which results in an apparent shift to smaller distance distribution values. The right panel is a zoom on the 4-6 nm region.

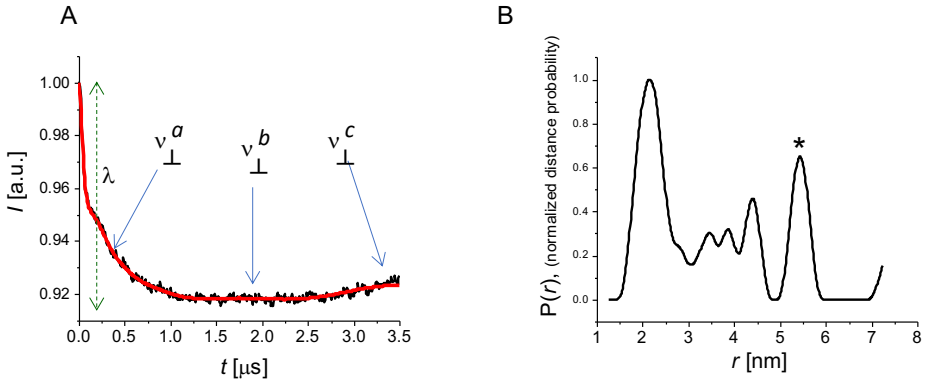

Figure 4 Supplement 3. Effect of the L6-barrel interaction on conformational changes of FhaC. (A) Dipolar evolution function for the PELDOR signal for FhaC$^{R492+195R1+503R1}$. (B) Distance distribution obtained by Tikhonov regularization of the signal depicted in (A). The asterisk corresponds to the longest distance measurable as a function of the *t* parameter applicable in this experiment.

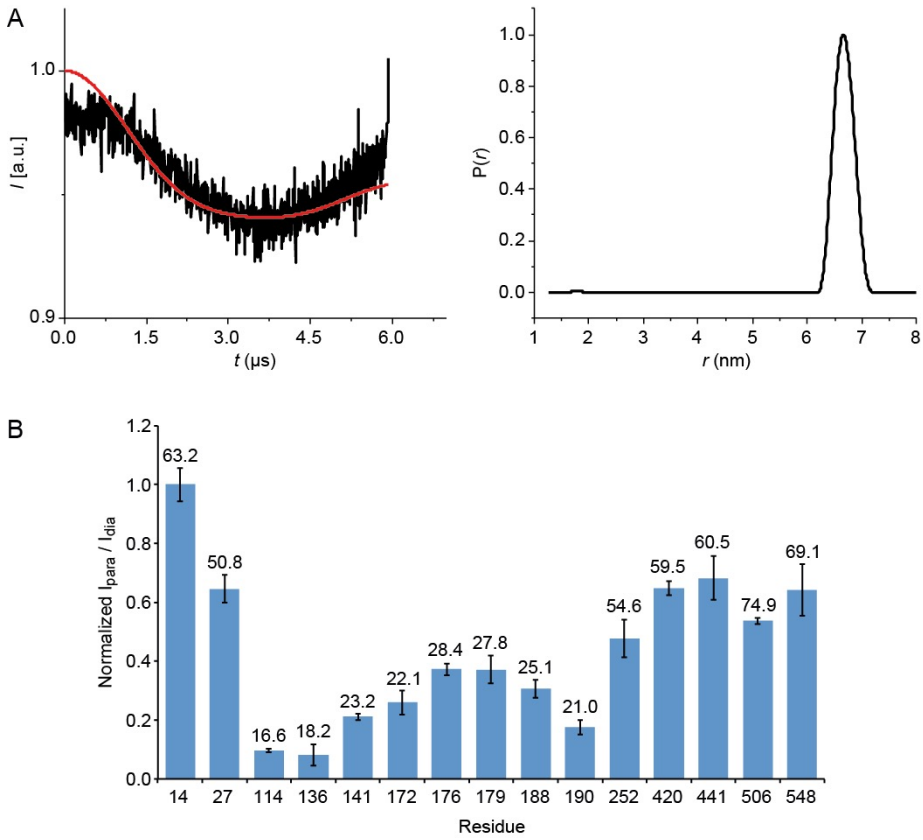

Figure 4 Supplement 4. Spectroscopic analyses of FhaC in nanodiscs. (A) Dipolar evolution function (*left*) and Tikhonov regularization (*right*) of the PELDOR signal of FhaC$^{195R1+503R1}$ in nanodiscs. (B) NMR paramagnetic relaxation enhancement experiments on FhaC^{195R1} in nanodiscs. Ratios I_{para}/I_{dia} of paramagnetic vs. diamagnetic FhaC^{195R1} Ile-δ_1 methyl peak intensities (normalized to their maximum value found for Ile^{14}; see Methods) extracted from ^{13}C-^{1}H heteronuclear multiple-quantum coherence (HMQC) experiments in solution before and after reduction of the MTSL spin label by addition of a 10-fold molar excess of ascorbic acid. Spectra were recorded on a 900 MHz spectrometer at 32°C. Error bars are calculated based on spectral noise levels. Numbers above the bars indicate the distance between the Cδ_1 nucleus of the corresponding Ile residue and the average position of the paramagnetic center in an ensemble of conformations of the MTSL tag attached to Cys^{195} in the FhaC crystal structure, calculated using the MtsslWizard PyMOL plugin (Hagelueken et al., 2012). Relative levels of signal attenuation due to the MTSL tag are perfectly in line with the relative distances of the corresponding residues from the paramagnetic center modeled onto the FhaC crystal structure, suggesting that FhaC in nanodiscs does not populate alternative conformations.

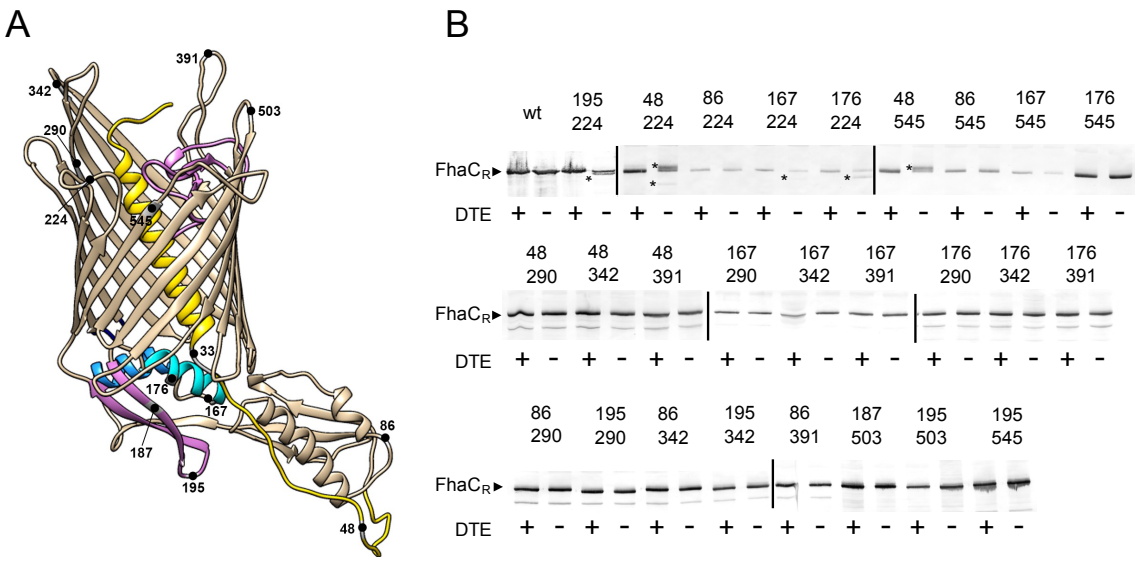

Figure 5. **Detection of transient conformers of FhaC *in vivo*.** (A) Position of the Cys substitutions in FhaC. (B) Immunoblot of membrane fractions of *E. coli JCB571* (*dsbA* KO strain) producing FhaC variants. The numbers indicate the positions of the two Cys residues. The reducing agent DTE was added to one half of each sample. FhaC$_R$ represents the position of the reduced form. The asterisks point to the additional, cross-linked forms that can migrate faster or more slowly than the reduced form, depending on the respective positions of the two Cys residues. S-S bond formation was confirmed by mass fingerprinting analyses (Figure Supplement 1).

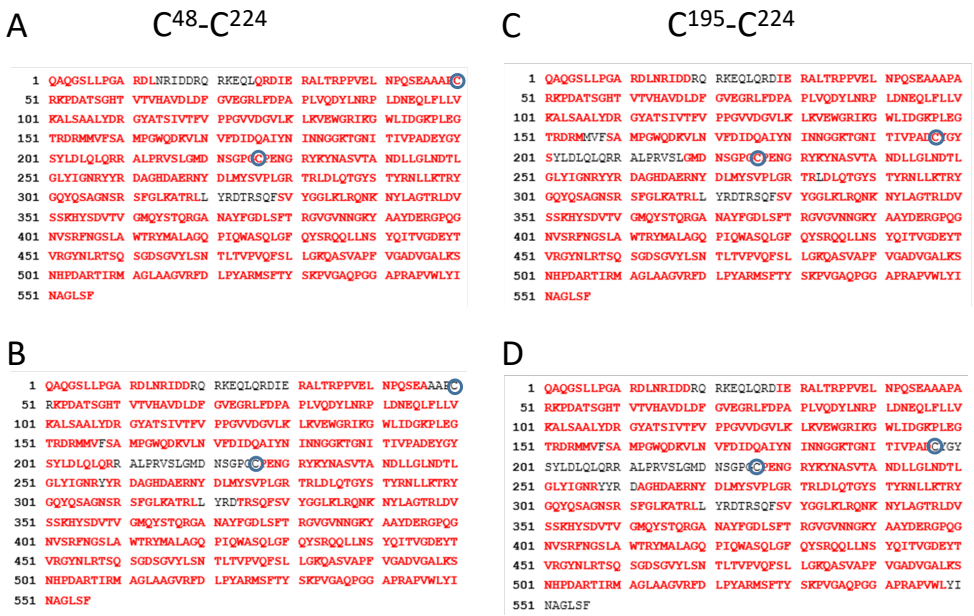

Figure 5 Supplement 1. Peptide mapping analysis of FhaC$^{C48-C224}$ and FhaC$^{C195-C224}$. Residues in red represent sequence coverage with (A,C) or without (B,D) reduction and alkylation. In the latter cases, the regions that contain the Cys residues were not characterized, suggesting the presence of an intramolecular S-S bond in both variants. Note that the sequences shown here contain an N-proximal Gly-Ser insertion for cloning purposes that has no effect on the structure or the activity of FhaC. The numbering of FhaC throughout the text corresponds to that of the native protein without this insertion.

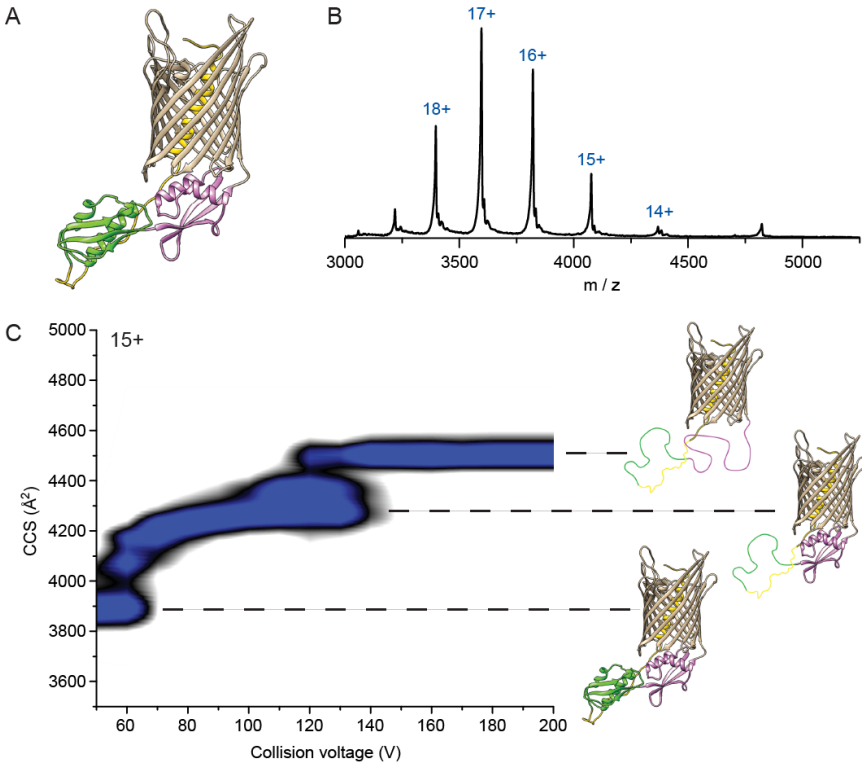

Figure 6. Native mass spectrometry analysis of WT FhaC. (A) Model of FhaC with H1 and the linker in yellow, and the POTRA domains 1 and 2 in pink and green, respectively. (B) Mass spectrum of WT FhaC released from its bOG micelle. The spectra at increasing collision energy are shown in Supplement 1. (C) Collision-induced unfolding (CIU) experiments show two dominant transitions that are likely linked to unfolding of the POTRA domains (see text), although the order in which they unfold is unknown. CIU profiles of control β-barrel proteins are shown in Supplement 2, and profiles of the $FhaC^{C4+C391}$ variant with H1 locked in the barrel are in Supplement 3.

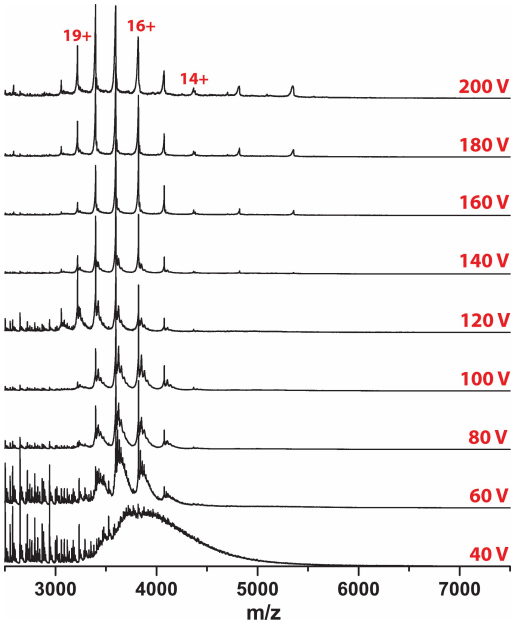

Figure 6 Supplement 1. Native MS analysis of FhaC in bOG micelles. The spectra were obtained at increasing collisional energy.

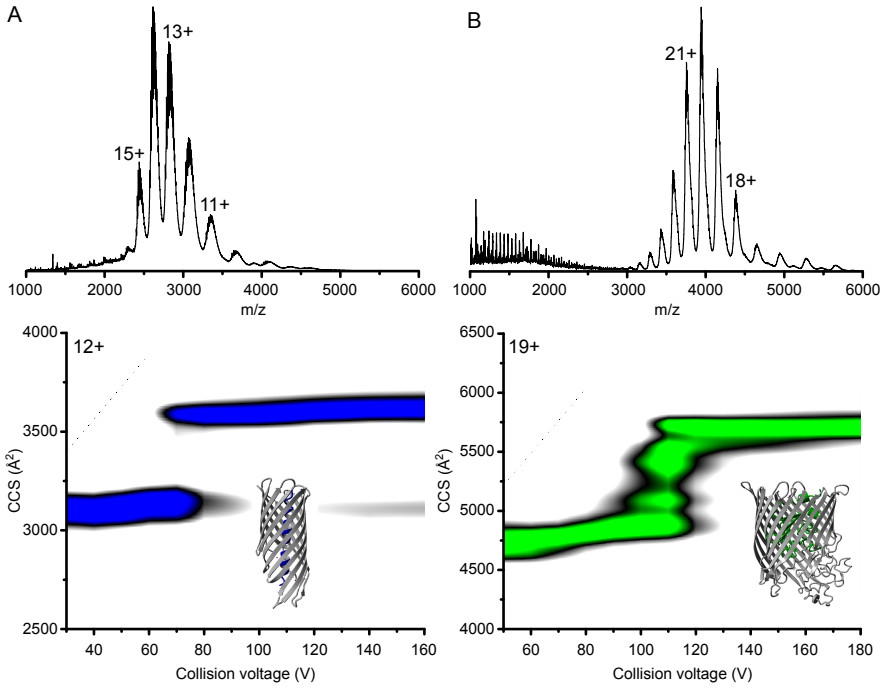

Figure 6 Supplement 2. Mass spectra and CIU plots of control OMPs. (A) SphB1-αβ is a truncated autotransporter (AT) containing only the β barrel with the preceding helical linker inserted in the barrel pore. (B) The TonB-dependent transporter BfrG is composed of a β barrel with a soluble N-terminal plug domain inserted in the barrel. The structural models shown are those of related transporters (PDB 1UYN and 3QLB, respectively), as the structures of SphB1-αβ and BfrG are not available. The mass spectra of the two OMPs released from their bOG micelles are shown at the top, and the CIU plots are below. Both show a single CIU transition, which suggests that the β barrels remain intact, while the soluble domains are ejected and unfold.

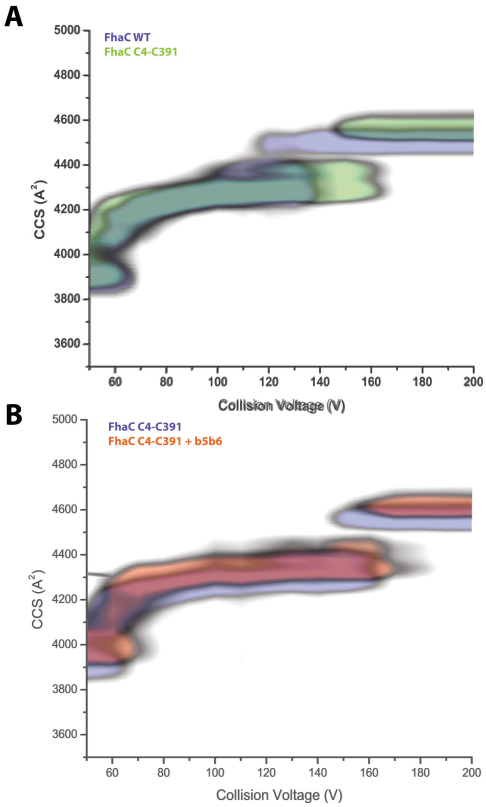

Figure 6 Supplement 3. CIU plots of FhaC$^{C4+C391}$. (A) Comparison of the CIU plots of wt FhaC (blue) and the FhaC$^{C4+C391}$ variant (green). (B) Overlay of the CIU plots of unbound FhaC$^{C4+C391}$ (blue) and FhaC$^{C4+C391}$ with the b5-b6 peptide bound (red). As for wt FhaC (see Figure 7), binding of the peptide to FhaC$^{C4+C391}$ increased CCS values at both low and high CE, suggesting that it induces enlargement of the β barrel, even with H1 inside.

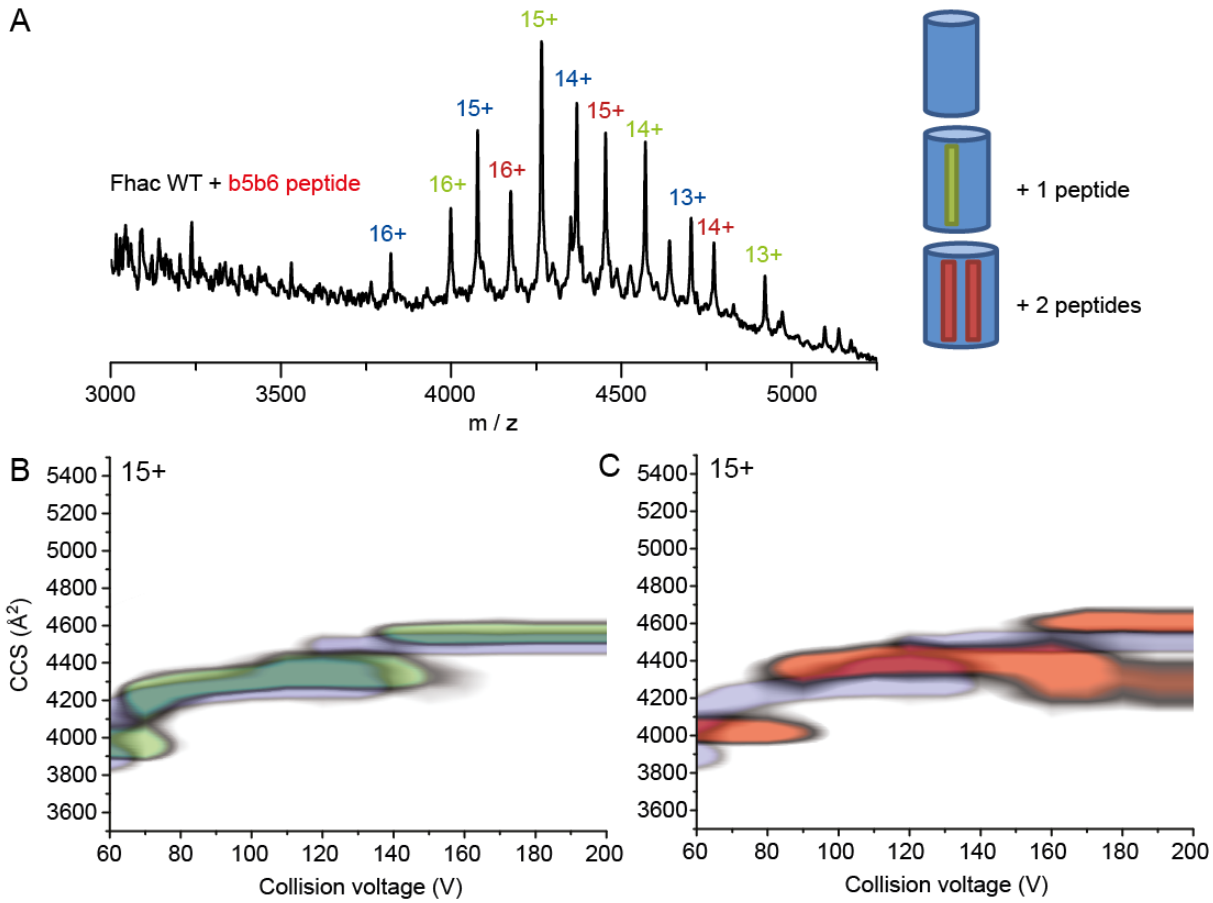

Figure 7. Binding of synthetic peptides to FhaC. (A) Mass spectrum of FhaC incubated with the b5-b6 peptide at a collisional energy of 150 V shows binding of the peptide to the protein under high-energy conditions. Schematic representations of the barrel with bound peptides are shown at the right. (B) Overlay of the CIU plots of FhaC with (green) and without (blue) one b5-b6 peptide bound. Increased CCS values are observed both under native conditions (low CE) and conditions in which the POTRA domains are most likely unfolded (high CE). (C) Comparison of the CIU plots of FhaC alone (blue) and FhaC with two b5-b6 peptides bound (orange), which shows an additional CCS increase compared to FhaC with a single peptide bound. The peptides used in this study are shown in Supplement 1. Binding of a different peptide and quantification of the binding data are shown in Supplement 2, the CIU plots of wt FhaC with the b4+L and Fha-NT peptides are shown in Supplement 3, and the CCS values measured in those experiments are in Supplement 4. The CIU plot of $FhaC^{C4+C391}$ with the b5-b6 peptide is shown in Figure 6 Supplement 3.

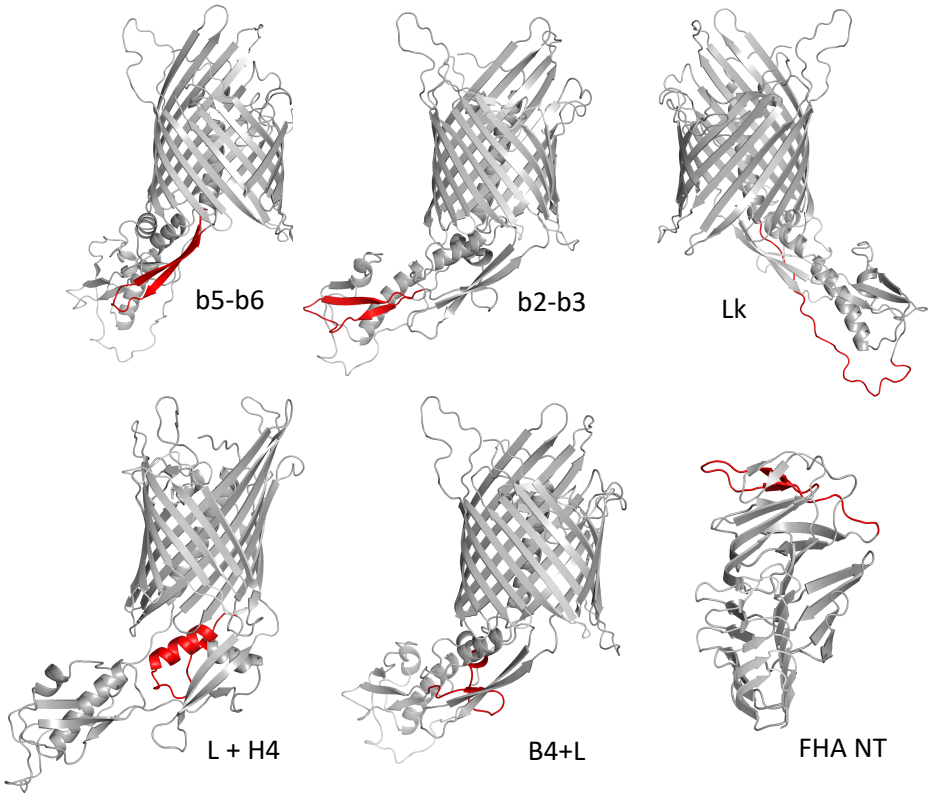

Figure 7 Supplement 1. Synthetic peptides used in this study. The first 5 peptides are shown in red on the structural model of FhaC, and the last one on the structural model of the N-terminal portion of FhaB (PDB 1RWR). The b5-b6 peptide (GKTGNITIVPADEYGYSYLDLQLQR) corresponds to the last two β strands of the POTRA2 domain that form an amphipathic β hairpin immediately preceding B1, the first strand of the β barrel. The b2-b3 peptide (SIVTFVPPGVVDGVLKLKVEWGR) encompasses the last two β strands of the POTRA1 domain. The Lk peptide (RPPVELNPQSEAAAPARKPDATSGH) corresponds to the linker between the H1 helix and the POTRA1 domain. The L+H4 peptide (AMPGWQDKVLNVFDIDQAIYNINNG) encompasses the loop (extended) region that precedes the H4 α helix and the H4 helix of the POTRA2 domain. The B4+L peptide (RIKGWLIDGKPLEGTRDR) corresponds to the β strand b4 of the POTRA2 domain followed by a loop region. Finally, the FHA-NT peptide (QTQVLQGGNKVPVVNIADPNS) corresponds to the N-terminal β strands b2 and b3 of FhaB forming a short hairpin, preceded and followed by loop regions.

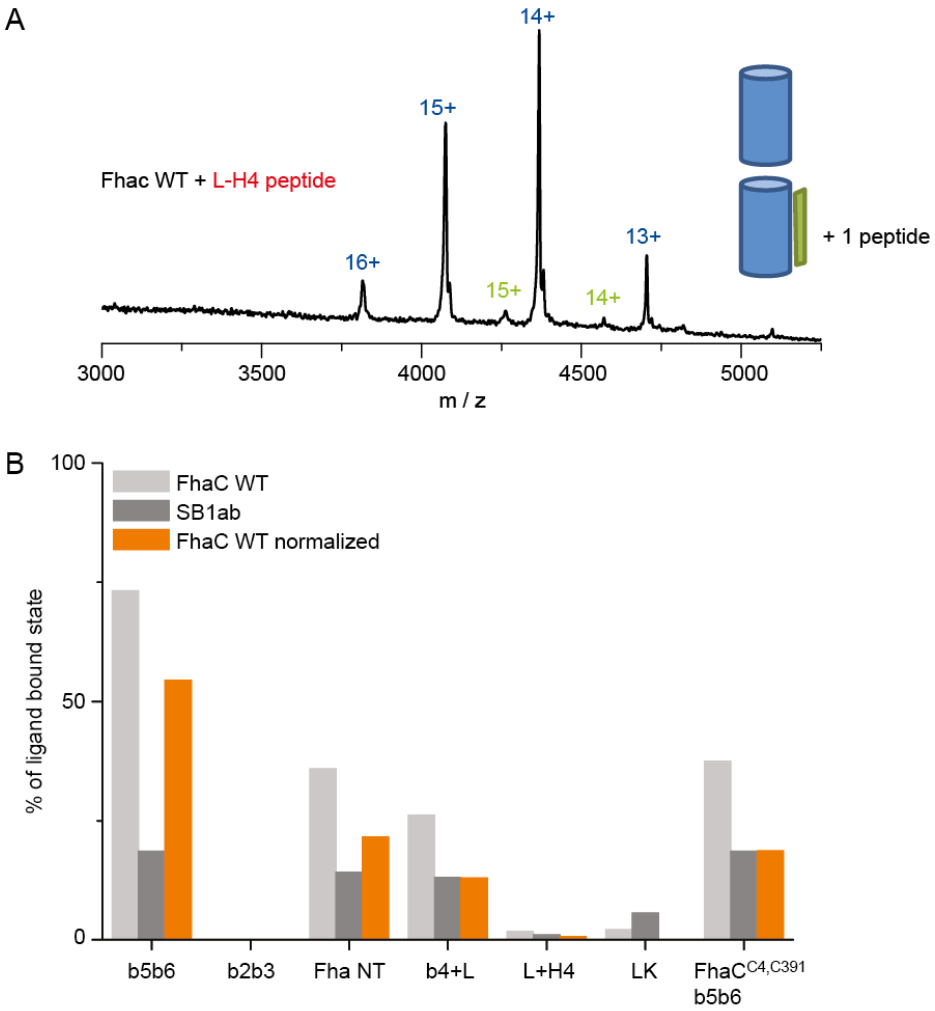

Figure 7 Supplement 2. Binding of synthetic peptides to FhaC. (A) Under similar conditions as in Fig. 7A (collisional energy of 150 V), only minimal binding was detected in the mass spectrum of FhaC incubated with the L+H4 peptide. (B) Quantification of the binding of synthetic peptides to FhaC (light grey) and to the control β-barrel protein SphB1-αβ (SB1ab, dark grey; used to correct for non-specific binding). Orange bars show normalized values.

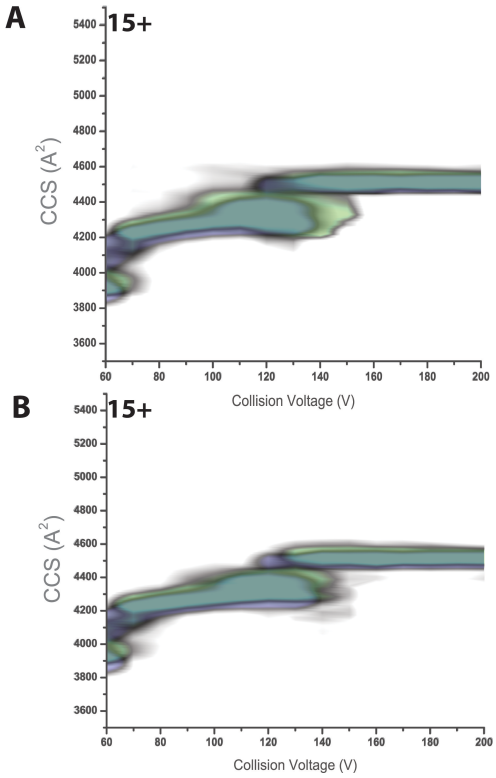

Figure 7 Supplement 3. CIU plots of FhaC incubated with synthetic peptides. (A) FhaC without (blue) or with (green) the Fha-NT peptide. (B) FhaC without (blue) or with (green) the B4+L peptide. In both cases the presence of the peptide caused an increased CCS at low collision voltage, but not at elevated collisional activation.

CCS (Å^2)	unbound	+1 peptide	+2 peptides
FhaC WT	3863/4502	-	-
+b5b6	-	3955/4556	4026/4595
+b4L	-	3954/4514	-
+Fha NT	-	3954/4515	-
FhaC C4-C391	3917/4555	-	-
+b5b6	-	3990/4607	ND/4646

Figure 7 Supplement 4. CCS of FhaC with various peptides determined at low and high CE (listed before and after the slash). The measured values indicate that only b5-b6 enlarges FhaC in both conditions.

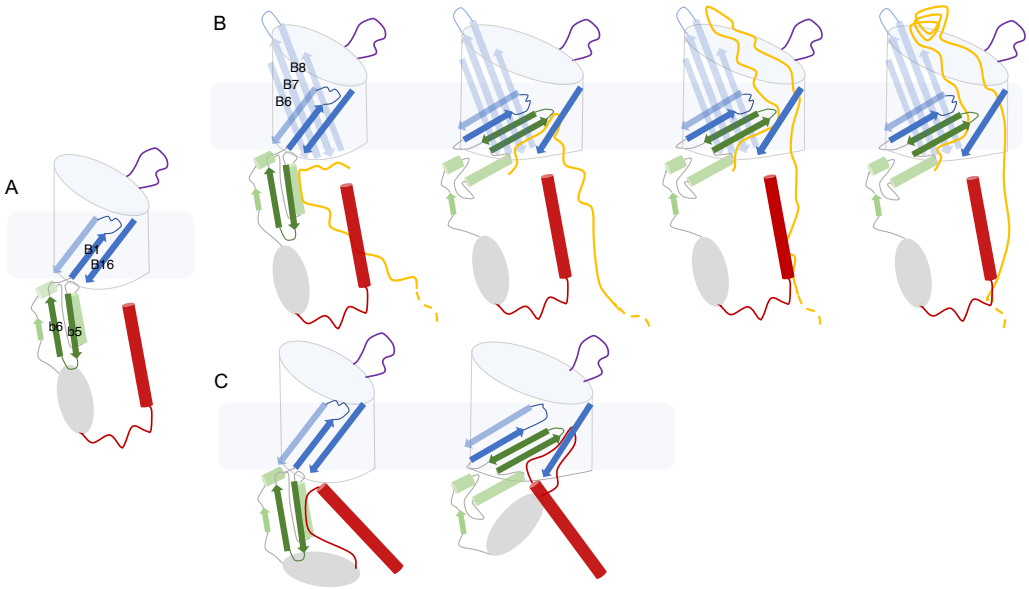

Figure 8. Model for TPS secretion. In the open conformation of FhaC (A), the substrate binding groove between H4 and b5 in the POTRA2 domain is available. (B) A specific region of the TPS domain of the substrate (yellow) binds to the POTRA2 domain, likely by β augmentation of the b5 strand. Unzipping of the barrel seam and insertion of the b5-b6 hairpin hoist a first portion of the substrate into the channel. The substrate likely forms a hairpin inside the barrel. Its diffusion toward the surface enables a specific portion of the TPS domain to interact with the B5-B8 beta sheet that protrudes at the cell surface. This interaction templates the folding of the substrate into a nascent β helix at the cell surface. The substrate is progressively threaded through the channel and folds at the surface, until a stable nucleus has formed. (C) In the absence of the substrate the linker binds to the POTRA2 domain, and the conformational changes of the protein can hoist it towards the cell surface in a futile cycle.